Spatial Distribution of Ca^{2+} Signals during Repetitive Depolarizing Stimuli in Adrenal Chromaffin Cells

Fernando D. Marengo and Jonathan R. Monck
Department of Physiology, UCLA School of Medicine, Los Angeles, California 90095

ABSTRACT Exocytosis in adrenal chromaffin cells is strongly influenced by the pattern of stimulation. To understand the dynamic and spatial properties of the underlying Ca^{2+} signal, we used pulsed laser Ca^{2+} imaging to capture Ca^{2+} gradients during stimulation by single and repetitive depolarizing stimuli. Short single pulses (10–100 ms) lead to the development of submembrane Ca^{2+} gradients, as previously described (F. D. Marengo and J. R. Monck, 2000, *Biophysical Journal*, 79:1800–1820). Repetitive stimulation with trains of multiple pulses (50 ms each, 2Hz) produce a pattern of intracellular Ca^{2+} increase that progressively changes from the typical Ca^{2+} gradient seen after a single pulse to a Ca^{2+} increase throughout the cell that peaks at values 3–4 times higher than the maximum values obtained at the end of single pulses. After seven or more pulses, the fluorescence increase was typically larger in the interior of the cell than in the submembrane region. The pattern of Ca^{2+} gradient was not modified by inhibitors of Ca^{2+}-induced Ca^{2+} release (ryanodine), inhibitors of IP_3-induced Ca^{2+} release (xestospongin), or treatments designed to deplete intracellular Ca^{2+} stores (thapsigargin). However, we found that the large fluorescence increase in the cell interior spatially colocalized with the nucleus. These results can be simulated using mathematical models of Ca^{2+} redistribution in which the nucleus takes up Ca^{2+} by active or passive transport mechanisms. These results show that chromaffin cells can respond to depolarizing stimuli with different dynamic Ca^{2+} signals in the submembrane space, the cytosol, and the nucleus.

INTRODUCTION

Ca^{2+} is a widely used intracellular signaling molecule that controls a large number of cellular processes (Berridge et al., 2000; Brini and Carafoli, 2000). Ca^{2+} controls short-term events on the millisecond timescale, such as synaptic transmission and muscle contraction, and also controls events that may last hours, such as transcription and synaptic long-term potentiation. The processes that Ca^{2+} controls are located in different parts of the cell, some near the plasma membrane, where they are particularly sensitive to Ca^{2+} entry, and some deep in the cell, where there may be delays in the signal transduction process. In addition, some Ca^{2+}-dependent processes are located in organelles, such as the mitochondria and nucleus, where the Ca^{2+} concentration might not be entirely independent of the cytosolic Ca^{2+} concentration but may change in a distinct way that depends on the dynamics and spatial organization of the cytosolic Ca^{2+} signal.

To understand how a particular cellular stimulus, electrical or chemical, regulates a large number of processes in an apparently distinct manner with high fidelity and without unnecessary crossover, we must understand the dynamics and the spatial organization of the Ca^{2+} signal. To do this, we must be able to measure Ca^{2+} at precise locations and at precise times, and in the case of excitable cells at early times. In practice it is difficult to do this for rapid events, as there is always a tradeoff between temporal resolution and spatial resolution. The best methods for measuring high resolution Ca^{2+} signals all have different tradeoffs. Thus, confocal spot detection gets excellent time resolution at a single optically limited location, whereas pulsed laser imaging gets high resolution spatial information at a single time; successive measurements can then be made at different locations or times, respectively (DiGregorio et al., 1999; DiGregorio and Vergara, 1997; Escobar et al., 1994; Marengo and Monck, 2000; Monck et al., 1994). Alternatively confocal line scan can get good time resolution, but the spatial information is limited to one direction (Hernández-Cruz et al., 1990; Nohmi et al., 1992; Segal and Manor, 1992). Each method has distinct advantages and disadvantages, and the most suitable technique will depend on the type of data required and the geometry of the cell. Even with these methods used under optimal conditions, there are still limitations. The amount of data that can be collected is limited by the high intensity laser illumination, the spatial resolution is limited by the optics of the microscope, and the pattern of Ca^{2+} signal is perturbed by the presence of the Ca^{2+} indicator, which binds significant amounts of Ca^{2+} and alters the dynamics of the spatial redistribution of Ca^{2+}.

A more recent approach is to use a combination of high-resolution Ca^{2+} measurement and mathematical modeling (e.g., Fink et al., 2000; Issa and Hudspeth, 1996; Marengo and Monck, 2000; Sala and Hernández-Cruz, 1990; Smith et al., 1998). The measurements of the dynamics and spatial distribution of the Ca^{2+} signal are used to build a virtual cell that can reproduce the measured pattern of Ca^{2+} changes. The model can then be used to interpolate between data

Submitted September 9, 2002, and accepted for publication May 19, 2003.

Address reprint requests to Jonathan R. Monck, Dept. of Physiology, Center for Health Sciences, 53-263, UCLA School of Medicine, 10833 Le Conte Ave., Los Angeles, CA 90095. Tel.: 310-825-0932; Fax: 310-206-3788; E-mail: jrmonck@mednet.ucla.edu.

Fernando D. Marengo's present address is Departamento de Fisiología y Biología Molecular, Facultad de Ciencias Exactas y Naturales, Universidad de Buenos Aires, Buenos Aires, Argentina.

0006-3495/03/11/3397/21 $2.00

points. More importantly, the model can also be used to extrapolate to situations that are not experimentally amenable, either to spaces very close to a Ca^{2+} channel or to predict the physiological Ca^{2+} signal in the absence of the Ca^{2+} indicator. In addition, the model can be used to help with experimental design or to make predictions about the properties of endogenous Ca^{2+} buffers or other cellular parameters.

Our interest in this approach came from our interest in the regulation of exocytosis by Ca^{2+} in adrenal chromaffin cells, where several phases of the process, including vesicle fusion from the readily releasable pool and vesicle mobilization to this pool, are thought to be Ca^{2+} dependent. In a previous study, using pulsed laser Ca^{2+} imaging, we found that, on opening of Ca^{2+} channels, the Ca^{2+} gradients develop relatively slowly, in terms of magnitude and rate of spread to the center of the cell (20–30 ms), and dissipate over hundreds of milliseconds, indicating that most of the Ca^{2+} is being bound to an immobile endogenous Ca^{2+} buffer (Marengo and Monck, 2000). By developing a model to explain the development of the Ca^{2+} gradient during the depolarizing pulse and the dissipation after the pulse we were able to make predictions about the properties of an endogenous poorly mobile high capacity Ca^{2+} buffer, and to estimate the kinetics of the Ca^{2+} signal near the cell membrane in the absence of Ca^{2+} indicator (Marengo and Monck, 2000).

Here we extend the study to consider the pattern of Ca^{2+} gradient development, dissipation, and clearance in response to repetitive (train) stimuli. We use the measured Ca^{2+} distributions to develop a virtual cell that can simulate the measured fluorescence changes. We were able to identify three spatially localized Ca^{2+} signals with distinct dynamic properties in adrenal chromaffin cells: a rapid Ca^{2+} spike just beneath the subplasma membrane, a cytosolic signal that increased in a stepwise fashion with each depolarizing pulse, and a slower, delayed increase in the nucleus.

METHODS

Cell preparation and solutions

Chromaffin cells were prepared from bovine adrenal medullae by enzymatic digestion (Burgoyne et al., 1988) and incubated 1–4 days in culture medium (Marengo and Monck, 2000). For experiments, chromaffin cells were washed in an extracellular medium comprising 120 mM NaCl, 20 mM Hepes, 4 mM $MgCl_2$, 5 mM $CaCl_2$, 5 mg/ml glucose, and 1 μM tetrodotoxin (pH 7.25). The standard internal solution used in the patch-clamp pipettes contained 125 mM Cs D-glutamate, 30 mM Hepes, 8 mM NaCl, 1 mM $MgCl_2$, 2 mM Mg-ATP, 0.3 mM GTP, 0.3 mM Cs-EGTA, and 0.2mM rhod-2 (pH 7.2). These solutions allow measurement of Ca^{2+} currents because Na^+ and K^+ currents are prevented. The holding potentials have not been corrected for junction potentials (Neher, 1992).

Measurement of Ca^{2+} gradients with pulsed laser imaging

Ca^{2+} gradients were measured using pulsed laser Ca^{2+} imaging of whole-cell patch-clamped cells, as previously described (Marengo and Monck, 2000; Monck et al., 1994). We used the Ca^{2+} indicator rhod-2 (Minta et al., 1989) and estimate the changes in Ca^{2+} concentration from the fractional fluorescence change (stimulus/control ratio, F_t/F_o) (Monck et al., 1988, 1994). We used a value of 1880 nM for the K_d (Escobar et al., 1997) and 0.013 for α (the ratio of the fluorescence of free and Ca^{2+}-bound rhod-2, determined in vitro using internal solution with "zero" Ca^{2+} (10 mM EGTA) and saturating Ca^{2+}, respectively). Assuming a value of 100 nM for the resting Ca^{2+} concentration, these values give Ca^{2+} concentrations of 240 and 410 nM for F_t/F_o values of 2 and 3, respectively (see Marengo and Monck, 2000, for a discussion of the calibration).

Simulation of the spatial organization of the Ca^{2+} signal

Mathematical model for Ca^{2+} entry, diffusion, and buffering

To simulate the changes in concentration of free Ca^{2+} and other species (e.g., free buffers and buffer-Ca^{2+} complexes) as a function of time and radial distance, we developed a radial diffusion model, which is described fully in Marengo and Monck (2000). This model assumes a uniform entry of Ca^{2+} through Ca^{2+} channels in a spherical cell, and is based on the model of Nowycky and Pinter (1993).

The cell is modeled as a sphere composed of concentric shells of equal thickness (0.1 μm). A simplifying assumption is that each shell represents a well-mixed system and that diffusion within the shell can be neglected. Diffusion of Ca^{2+} and buffers is assumed to occur solely at the shell interfaces and can be described by a function involving shell thickness (i.e., diffusional distance), shell surface areas (inner and outer), and diffusion coefficient. Given these assumptions, Eq. 1 can be represented as a system of first-order, ordinary differential equations describing the concentration of Ca^{2+} (and other diffusible species) in each shell, where the first shell is the outer shell and the Nth shell is the innermost. For the ith shell of N shells, the diffusion equation takes the form:

$$\frac{d[Ca^{2+}]}{dt} = \frac{D_{Ca}}{V_i\delta}\left(A_{i-1}P_{i-1}\left([Ca^{2+}]_{i-1} - [Ca^{2+}]_i\right) - A_iP_i\left([Ca^{2+}]_i - [Ca^{2+}]_{i+1}\right)\right), \quad (1)$$

where $[Ca^{2+}]_i$ is the concentration of free Ca^{2+} in the ith shell, D_{Ca} is the diffusion coefficient for Ca^{2+}, δ is the shell thickness, V_i the shell volume, and A_i and A_{i-1} are the surface areas of the inner and outer surfaces of the ith shell. P_i is a permeability factor for each shell surface; the value ranges from zero, to represent an impermeable membrane, to 1, to represent free diffusion. So for most shell surfaces where there is no membrane or boundary condition, $P_i = 1$. The boundary conditions specify that diffusion does not occur across the outermost spherical boundary or out of the innermost shell, which is spherical. The boundary conditions were achieved by setting P_0 (outer boundary of first shell) and P_N (inner boundary of Nth shell) to zero.

The permeability factor is also used to make a membrane permeable to one or more species. We used this to make the nuclear membrane permeable to Ca^{2+} and mobile Ca^{2+} buffers (see below) and for making the plasma membrane permeable to Ca^{2+} in the presence of ionomycin. In addition, the permeability factor was used to simulate diffusion between the pipette solution and the cytosol by making the plasma membrane partially permeable (in proportion to the pipette tip size). We assumed that the pipette-cytosol exchange is relatively slow and that we could simulate the diffusional exchange between the pipette and the outer shell of the cytosol as a simple two-compartment model.

The final model also includes components for Ca^{2+} entry through Ca^{2+} channels, Ca^{2+} leak, and Ca^{2+} extrusion, and for Ca^{2+} binding to mobile and immobile Ca^{2+} buffers. The following is a first-order differential equation to describe the change in Ca^{2+} concentration in each shell:

$$\frac{d[Ca^{2+}]}{dt} = \frac{D_{Ca}}{V_i\delta}(A_{i-1}P_{i-1}([Ca^{2+}]_{i-1} - [Ca^{2+}]_i) - A_iP_i([Ca^{2+}]_i - [Ca^{2+}]_{i+1}))\cdots + \left(\frac{d[Ca^{2+}]_i}{dt}\right)_{B^A} + \left(\frac{d[Ca^{2+}]_i}{dt}\right)_{B^B} + \left(\frac{d[Ca^{2+}]_i}{dt}\right)_{B^C}\cdots + \left(\frac{d[Ca^{2+}]_i}{dt}\right)_{I_{Ca}} + \left(\frac{d[Ca^{2+}]_i}{dt}\right)_{Leak} + \left(\frac{d[Ca^{2+}]_i}{dt}\right)_{Pump}. \quad (2)$$

The three terms of the form $d[Ca^{2+}]_i/dt)_B{}^x$ represent the change in Ca^{2+} concentration due to binding to three Ca^{2+} binding buffers (B^A–B^C), which is calculated with the equation: $(d[Ca^{2+}]_i/dt)^x_B = k_{-1}[CaB^x] - k_{+1}[Ca^{2+}][B^x]_i$, where $[CaB^x]$ is the concentration of Ca^{2+} bound to buffer X, $[B^x]$ is the concentration of unbound buffer, and k_{+1} and k_{-1} are the forward and reverse rate constants for the binding of Ca^{2+} to the buffer. The three Ca^{2+} buffers considered are the Ca^{2+} indicator, EGTA, and endogenous buffer. The last three terms, for Ca^{2+} influx, leak, and extrusion, are only present in the outer shell, i.e., they are zero when $i \neq 1$. A set of similar equations can be developed for the change in the concentration of Ca^{2+}-buffer complex and free buffer for each diffusible buffer:

$$\frac{d[CaB^x]}{dt} = \frac{D_x}{V_i\delta}(A_{i-1}P_{i-1}([CaB^x]_{i-1} - [CaB^x]_i) - A_iP_i([CaB^x]_i - [CaB^x]_{i+1})) + \left(\frac{d[CaB^x]_i}{dt}\right) \quad (3)$$

$$\frac{d[B^x]}{dt} = \frac{D_x}{V_i\delta}(A_{i-1}P_{i-1}([B^x]_{i-1} - [B^x]_i) - A_iP_i([B^x]_i - [B^x]_{i+1})) + \left(\frac{d[B^x]_i}{dt}\right). \quad (4)$$

Equation 4 is different from that used previously (Marengo and Monck, 2000), where we make the additional assumption that the diffusion coefficients for Ca^{2+}-buffer complex and unbound buffer are equal, so that the total concentration of buffer in each shell is constant and equal to the initial total concentration of buffer. Using this assumption eliminated the need to have a set of equations for the change in concentration of unbound buffer (so Eq. 4 simplified to$[B^x] = [B^x_{total}] - [CaB^x]$). The current modification was made to enable us to explore the effect of alternating the restricted diffusion across the nuclear membrane using relative permeabilities.

For selection of values for diffusion coefficients, affinities, and kinetic properties of exogenous and endogenous Ca^{2+} buffers, we used the same values that we previously determined to best simulate the measured Ca^{2+} gradients (Marengo and Monck, 2000). Thus we used 100 $\mu m^2 \cdot s^{-1}$ for the diffusion coefficient for rhod-2 and Ca^{2+}, 800 for the buffer capacity of endogenous buffer, which was assumed to have a K_d of 1 μM and a dissociation rate constant of 0.05 ms^{-1}. As this buffer is assumed to be immobile, the diffusion coefficient was set to zero. In some simulations, the endogenous Ca^{2+} buffer exhibited positive cooperativity. In these cases, the endogenous buffer was given four Ca^{2+} binding sites, with the same properties as used before and keeping the total number of binding sites constant. For this we set up equations for three additional equilibria: Ca^{2+} binding to buffer with one, two, or three sites occupied. By increasing the affinity of the Ca^{2+} binding to buffer with three occupied sites, we were able to simulate positive cooperativity. For the simulations in Fig. 7, *B* and *C*, the affinity of this site was increased to 10 nM. We used a Ca^{2+} current of 210 pA, as previously determined (Marengo and Monck, 2000). Ca^{2+} channel rundown was simulated empirically from the measured decrease in Ca^{2+} current with pulse number. For example, the Ca^{2+} currents were reduced to 88.6 ± 1.33% ($n = 15$) and 74.0 ± 2.1% of the initial values after 5 pulses and 10 pulses, respectively. All other Ca^{2+} buffer and Ca^{2+} transport parameters were as given in Marengo and Monck (2000).

Equations 2–4 were numerically integrated using a first-order Euler algorithm written in Visual Basic 6.0 (Microsoft, Redmond, WA). Simulations usually required an integration time step of 2–10 μs. Further details of the model are given in Marengo and Monck (2000).

Simulation of the Ca^{2+} signal in the nucleus

A nucleus centered on the center of the cell was simulated by introducing a barrier between two shells at the appropriate location (usually 40 shells from the cell surface, giving a nuclear radius of 2.1 μm). This barrier was either completely impermeable or given a partial permeability by changing the permeability factor for the surface representing the position of the nuclear membrane, e.g., for 1% of free diffusion we used $P_{Nuc} = 0.01$ (subscript ''Nuc'' refers to the position of the nucleus, i.e., when $i = 40$). In some cases, the permeability of the nuclear membrane to Ca^{2+}-bound indicator was set to different values depending on whether the diffusion was into or out of the nucleus. In this case, Eq. 4 was modified as follows:

$$\frac{d[CaB^x]}{dt} = \frac{D_x}{V_i\delta}(A_{i-1}P_{i-1}[CaB^x]_{i-1} - A_{i-1}P_{i-1}[CaB^x]_i - A_iP_i[CaB^x]_i + A_iP_i[CaB^x]_{i+1}) + \left(\frac{d[CaB^x]_i}{dt}\right) \quad (5)$$

and where P_{Nuc} was modified depending on the direction of movement. This modification allowed us to explore some passive mechanisms for changes in nuclear Ca^{2+} concentration.

Active nuclear Ca^{2+} transport was modeled using first-order processes dependent on Ca^{2+} on the cytosolic side and nuclear side of the membrane:

$$\left(\frac{d[Ca^{2+}]}{dt}\right)_{NucUp} = -V^{up}_{max}A_{Nuc}[Ca^{2+}]_{Nuc-1}/V_{Nuc-1}([Ca^{2+}]_{Nuc-1} + K^{up}_m) \quad (6)$$

$$\left(\frac{d[Ca^{2+}]}{dt}\right)_{NucEff} = -V^{eff}_{max}A_{Nuc}[Ca^{2+}]_{Nuc}/V_{Nuc}([Ca^{2+}]_{Nuc} + K^{eff}_m), \quad (7)$$

where V_{max} and K_m are the maximum rate and the Michaelis-Menten constants for the Ca^{2+}-uptake (superscript ''Up'') and efflux (superscript ''Eff'') processes, and the subscript ''Nuc − 1'' refers to the last cytosolic shell before the nuclear membrane and the subscript ''Nuc'' refers to the first nuclear shell (the inner surface of this shell, A_{Nuc}, represents the nuclear membrane). No assumptions about the mechanism are made, apart from the first-order Ca^{2+} dependence. To provide a steady-state Ca^{2+}, a constant leak was defined as being equal and opposite to the net Ca^{2+} transport determined by the steady-state Ca^{2+} uptake and efflux at the resting cytosolic Ca^{2+} concentration, calculated using Eqs. 6 and 7.

We also incorporated binding of Ca^{2+} indicator to nuclear constituents, designated as indicator binding constituent (IBC). For this we set up equations for three additional eqiuilibria: binding of free indicator (B^D) to IBC, binding of Ca^{2+} indicator complex (CaB^D) to IBC, and Ca^{2+} binding to indicator bound to IBC. As these three equilibria form a cycle with the

Ca^{2+} binding to free indicator, we ran the simulation to achieve a new steady-state before initiating Ca^{2+} entry through Ca^{2+} channels.

Simulating the fluorescence changes and the blurring introduced by the optics

The fluorescence, F, of a fluorescent indicator dye is given by

$$F^{D} \propto \alpha[B^{D}] + [CaB^{D}], \quad (8)$$

where α is the ratio of the fluorescence of the free (B^{D}) and Ca^{2+}-bound (CaB^{D}) species of the indicator. The proportionality constant drops out when the fractional fluorescence change (F_t/F_0) is calculated.

An important component of the model is that it is directly comparable with the measured fluorescence data. However, we cannot directly compare the fluorescence simulations with the experimental images because the observed fluorescence images were obtained with an epifluorescence microscope and are contaminated with out-of-focus information. On the other hand, the simulations provides a ''nonblurred'' ideal representation of the fluorescence gradients. Therefore, to allow a better comparison with experimental data, we constructed a three-dimensional model of the fluorescence simulations and ''blurred'' it using the theoretical point spread function of the microscope, as previously described (Marengo and Monck, 2000; Monck et al., 1992).

RESULTS

We studied the pattern of Ca^{2+} distribution during single and repetitive depolarizing stimuli in patch-clamped adrenal chromaffin cells loaded with fluorescent Ca^{2+} indicators. We used pulsed laser Ca^{2+} imaging to capture Ca^{2+} gradients, which were measured as dynamic fluorescence ratios (F_t/F_o) between the image obtained after the single or multiple depolarizing pulses and an image obtained just before the start of the stimulus.

Ca^{2+} gradients during single and repetitive depolarizing pulses

Fig. 1 shows the pattern of Ca^{2+} distribution after stimulation of patch-clamped adrenal chromaffin cells with different numbers of depolarizing pulses, 50 ms steps from −70 mV to +20 mV at 500 ms intervals (2 Hz). As we have shown before (Marengo and Monck, 2000; Monck et al., 1994), the pattern after a single pulse is a prominent submembrane Ca^{2+} gradient (Fig. 1, *A* and *B*, *left*), with the

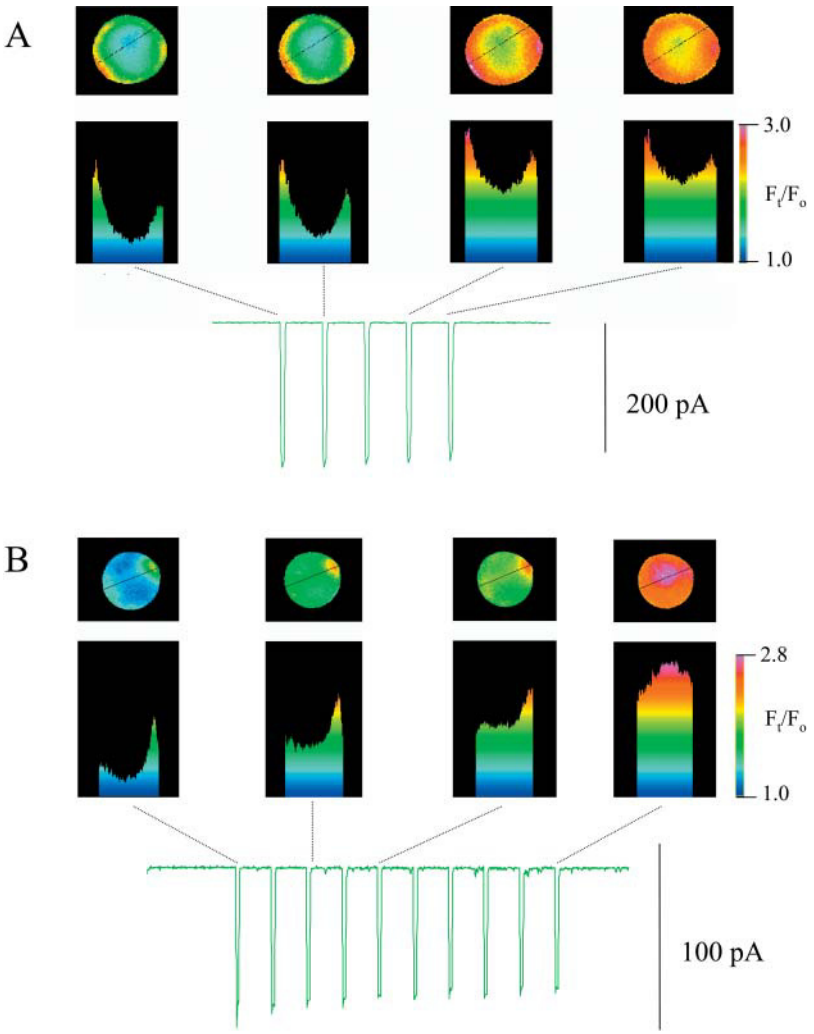

FIGURE 1 Dynamics of Ca^{2+} distribution during repetitive depolarizing stimuli. Ca^{2+} images and Ca^{2+} currents were measured during a train of 10 depolarizing pulses (50 ms duration, from −70 to +20 mV at 500 ms intervals (2 Hz)). (*A*) Dynamic fluorescence ratios representing the Ca^{2+} distribution after 1, 2, 4, and 5 pulses. (*B*) Dynamic fluorescence ratios captured after 1, 3, 5, and 10 pulses in a different cell. Fluorescence images were captured before the stimuli (control) and immediately after the pulses (stimulus image) using a pulsed laser imaging protocol (see Methods). Below each image is the fluorescence cross-sectional profile, measured along the black line shown superimposed on the images. Assuming a value of 100 nM for the resting Ca^{2+} concentration, F_t/F_o values of 2 and 3 give Ca^{2+} concentrations of 240 and 410 nM, respectively. Note how the prominent Ca^{2+} gradient apparent after a few pulses is gradually replaced by a more global increase. After 10 pulses, there is a prominent increase in the cell interior. This is typically seen after 7 or more pulses. More examples of the Ca^{2+} distribution after 10 pulses are shown in Fig. 2.

Ca^{2+} decreasing progressively toward the center of the cell, where there was only a small increase. These Ca^{2+} distributions can be accounted for by Ca^{2+} entry, binding to buffers and by diffusion of Ca^{2+} and the Ca^{2+} buffers, as described in detail (Marengo and Monck, 2000). There is no contribution from Ca^{2+} and IP_3-sensitive intracellular Ca^{2+} stores, as the changes are not affected when intracellular stores are inhibited or depleted. Inhibition of Ca^{2+} and IP_3-induced Ca^{2+} release with ryanodine (five cells) or xestospongin (three cells) resulted in maximum fluorescence changes at the cell border of 1.92 ± 0.12 and 2.06 ± 0.12, respectively, compared to 1.94 ± 0.12 for controls (13 cells). Likewise, the cellular spatial averages were 1.50 ± 0.09, 1.60 ± 0.02, and 1.49 ± 0.06 with ryanodine, xestospongin, and in control cells. In addition, when thapsigargin ($n = 6$) was added to reduce endoplasmic reticulum Ca^{2+} content, no changes were observed in comparison with control condition (1.87 ± 0.18 and 1.44 ± 0.12 for the maximum signal at border and spatial average, respectively), in agreement with our previous study.

When the cell was stimulated with 2–5 depolarizing stimuli, Ca^{2+} gradients near the cell membrane were still clearly visible, with the maximal fluorescence change at the edge increasing with pulse number, but the increase in the center of the cell becomes progressively larger so that the edge to center gradient is less prominent (Fig. 1). After seven or more pulses, the fluorescence increase was typically larger at a region within the cell interior that peaks at values 2–4 times higher than the maximum values obtained at the end of single pulses (Fig. 1 *B*, *right*). This type of pattern was observed in 21 cells. Several more examples of the fluorescence changes after 10 pulses are shown in Fig. 2.

Colocalization of large central increase with nucleus

We compared the bright-field images of the cells with the dynamic fluorescence ratios representing the spatial distribution of the Ca^{2+} change after repetitive stimulation, to examine whether the large interior increase is colocalized with a particular cellular structure. Fig. 2 shows four examples (*A–D*) where there is a spatial coincidence of the largest fluorescence increase with nuclear region. When the nucleus was clearly visible in the bright-field images, we always observed this colocalization after stimulation with a train of 10 pulses of 50 ms duration at 2Hz ($n = 18$, in 13 cells).

Fig. 3 shows an analysis of the fluorescence changes in the cytosolic and nuclear regions, as well as the cellular spatial average. The data are pooled from a number of cells, after stimulation with different numbers of depolarizing pulses. Analysis of the fluorescence changes in the cytosolic and nuclear regions from data recorded from nine cells shows that the nuclear signal lags behind the cytosolic signal for the first five pulses and then becomes larger thereafter (Fig. 3 *A*). The F_t/F_o values in the ''nuclear region'' and the ''cytosolic region'' of the cell after 10 pulses were 3.18 ± 0.17 and 2.75 ± 0.12, respectively, and the difference was highly significant (0.43 ± 0.06, $p < 0.001$, $n = 19$). Most of the variation is due to differences in the size of the changes observed in different cells, as the relative time courses of the cytosolic and nuclear fluorescence changes can be seen more clearly when the data are normalized by expressing the changes in the cytosol and nucleus as a percentage of the spatially averaged change throughout each cell (Fig. 3 *B*).

The data in Fig. 2 clearly show that the larger increase in the cell interior colocalizes with the nucleus, which is consistent with previous reports of a larger Ca^{2+} increase in the nucleus (e.g., Williams et al., 1985). This observation could be because the nucleus contains a distinct Ca^{2+} compartment that has a slowly developing large increase. Alternatively, there might be Ca^{2+} release from perinuclear intracellular Ca^{2+} stores. The perinuclear region in adrenal chromaffin cells is rich in endoplasmic reticulum with IP_3-sensitive Ca^{2+} stores (Burgoyne et al., 1989; O'Sullivan et al., 1989). Thus IP_3-induced Ca^{2+} release from the

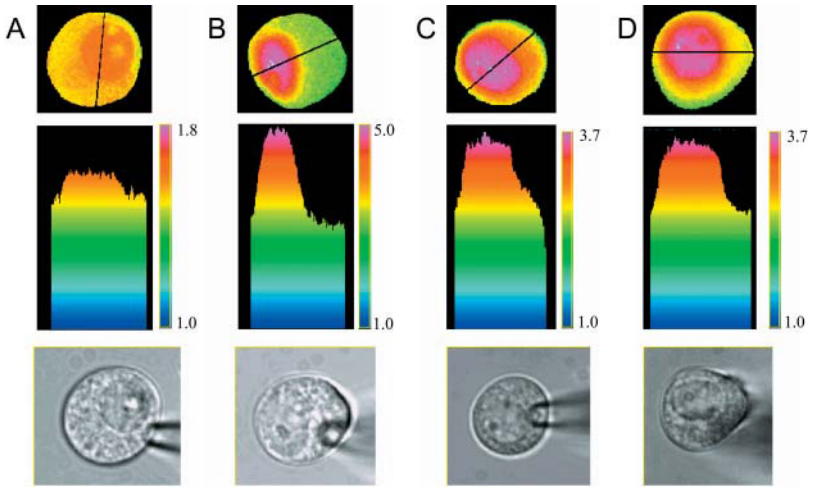

FIGURE 2 The Ca^{2+} increase in the cell interior colocalizes with the nucleus. The distribution of Ca^{2+} signal was measured after 10 depolarizing pulses (50 ms duration, from −70 to +20 mV) in four different cells. (*Top*) Dynamic ratio images, representing the change in Ca^{2+} distribution, along with corresponding cross-sectional profiles through cell. (*Bottom*) Bright-field images of the same cells showing the nucleus. The fluorescence images were captured just after the 10th pulse (*A*, *B*, and *C*) or just before the 10th pulse (*D*). The cells in *A*, *C*, and *D* were stimulated at 2 Hz and the cell in B at 1 Hz. Assuming a value of 100 nM for the resting Ca^{2+} concentration, F_t/F_o values of 1.8, 3.7, and 5.0 give Ca^{2+} concentrations of 210, 540, and 830 nM, respectively. Note how the large fluorescence increase appears to colocalize with the position of the nucleus.

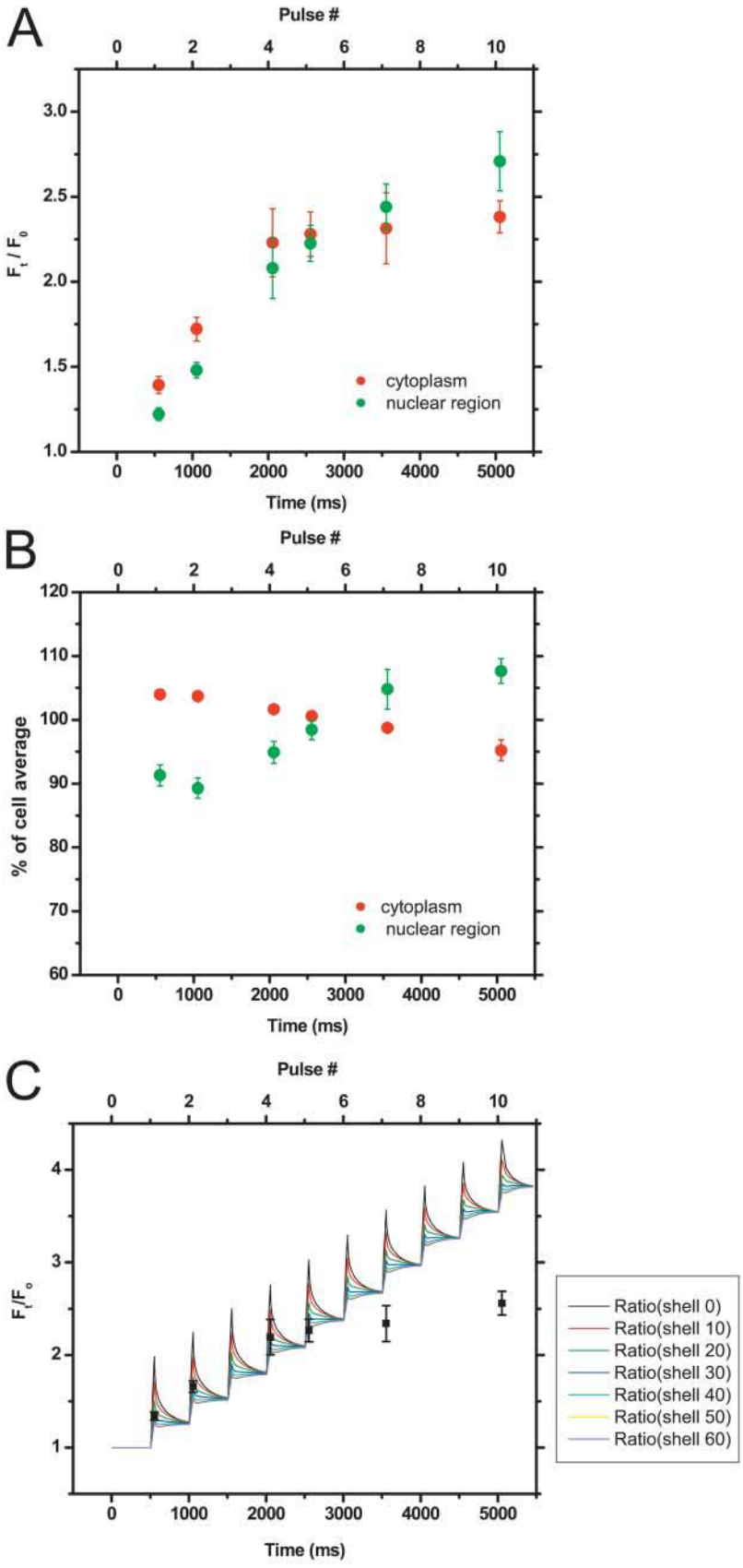

FIGURE 3 Analysis of fluorescence changes during repetitive stimulation. The average fluorescence changes in the whole cell, and the cytosolic and nuclear regions, were measured from images like those shown in Figs. 1 and 2. (*A*) Average fluorescence changes in the cytoplasm (*red circles*) and the nuclear region (*green circles*) after different numbers of pulses during 2 Hz stimulation with 50 ms depolarizing pulses. The data were analyzed from recordings in nine cells, but not every time point was taken in all cells (1 pulse, $n = 6$; 2 pulses, $n = 5$; 4 pulses, $n = 3$; 5 pulses, $n = 5$, 7 pulses, $n = 3$; 10 pulses, $n = 7$). (*B*) Relative changes in the cytosol and nucleus after normalization for the size of the average fluorescence change in each cell. The changes in the cytosol and nucleus were calculated as a percentage of the spatially averaged change measured throughout each cell before averaging the data for different cells. The lower variation seen after this normalization indicates that most of the variation observed in *A* is due to differences in the size of the changes observed in different cells. Note that in several cases, the error bars are within the size of the symbols. (*C*) Cell average data superimposed over the simulated fluorescence gradients (after blurring to allow a realistic comparison) using the model previously developed (Marengo and Monck, 2000). Note that the measured fluorescence increase appears to saturate after 5 or 6 pulses, which is not accounted for in this version of the model.

endoplasmic reticulum or from the nuclear envelope, which has been shown to support similar Ca^{2+} release (Gerasimenko et al., 1995; Stehno-Bittel et al., 1995), might explain the larger fluorescent increase in the nuclear region. However, it might be difficult to definitively distinguish between a Ca^{2+} increase in the nucleus and an increase occurring due to release of Ca^{2+} in the perinuclear region because of the contaminating out-of-focus light in our fluorescent images. To address this issue, we investigate the possible role of intracellular Ca^{2+} stores in the next section using a pharmacological approach.

Role of intracellular Ca^{2+} stores

To study the possibility that the prominent F_t/F_o increase in the cell interior was due to Ca^{2+} release from intracellular stores, we performed a series of experiments using specific inhibitors (Fig. 4). First, the characteristic pattern of a significantly larger Ca^{2+} increase in the nuclear region was not modified qualitatively when the endoplasmic reticulum was depleted with thapsigargin, an inhibitor of reticular Ca^{2+}-ATPases (eight measurements obtained in five cells). Second, we observed the same pattern when Ca^{2+}-induced Ca^{2+} release was inhibited with ryanodine (10 measurements obtained in 5 cells). Third, the pattern was also unaffected when IP_3 induced Ca^{2+} release was blocked with xestospongin (four measurements in four cells). In addition, inhibition of mitochondria with FCCP plus oligomycin, which will inhibit mitochondrial uptake and deplete any mitochondrial Ca^{2+} stores, had no effect on the pattern of Ca^{2+} distribution (nine measurements in six cells). This latter result is complicated by the fact that the FCCP/oligomycin treatment inhibits the Ca^{2+} current, since the integral of I_{Ca} during the train in these experiments was 66 ± 11 pC ($n = 6$), compared to 98 ± 12 ($n = 21$) in controls. However, although this resulted in a reduction of the spatially averaged Ca^{2+} signal in presence of FCCP (1.94 ± 0.30, $n = 6$, compared to 2.77 ± 0.16, $n = 21$, for the controls), the large intracellular Ca^{2+} increase in the nuclear region was still observed.

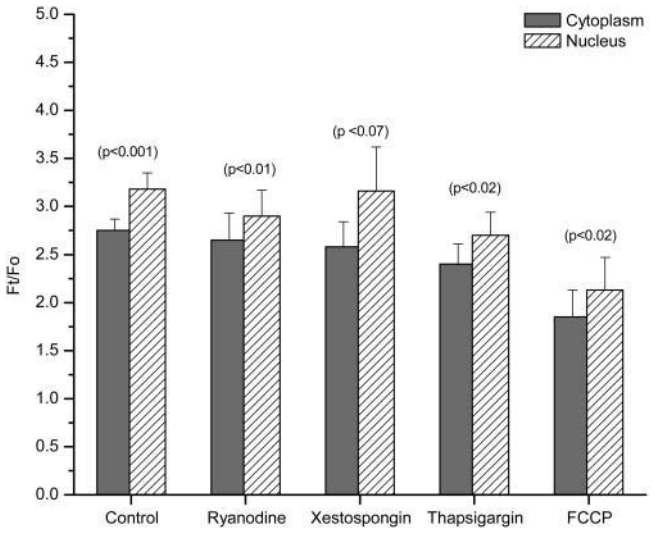

FIGURE 4 The Ca^{2+} increase in the vicinity of the nucleus is not due to Ca^{2+} release from perinuclear Ca^{2+} stores. Histogram of average fluorescence changes for the cytoplasm and the region containing the nucleus under various pharmacological treatments: control; ryanodine (1 mM), to inhibit Ca^{2+}-induced Ca^{2+} release; xestospongin (10 μM), to inhibit IP_3 sensitive stores; thapsigargin (1 μM), to inhibit Ca^{2+} uptake into reticular stores; and FCCP (1 μM with the addition of 0.2 μM oligomycin), to prevent uptake and release of Ca^{2+} by mitochondria. The F_t/F_o values for the nuclear and cytosolic regions after 10 pulses were 3.18 ± 0.17 and 2.75 ± 0.12, respectively for controls (difference 0.43 ± 0.06, $p < 0.001$, $n = 19$), 2.90 ± 0.27 and 2.65 ± 0.28 for ryanodine (difference 0.25 ± 0.03, $p < 0.01$, $n = 5$), 3.16 ± 0.46 and 2.58 ± 0.26 for xestospongin (difference 0.57 ± 0.20, $p < 0.07$, $n = 4$), 2.70 ± 0.24 and 2.40 ± 0.21 for thapsigargin (difference 0.29 ± 0.07, $p < 0.02$, $n = 5$), and 2.13 ± 0.34 and 1.85 ± 0.28 for FCCP (difference 0.28 ± 0.08, $p < 0.02$, $n = 6$).

Since the pattern of the large intracellular Ca^{2+} increase in the vicinity of the nucleus was not abolished by addition of thapsigargin, ryanodine, xestospongin, or FCCP plus oligomycin (Fig. 4), it seems unlikely that the Ca^{2+} increase in the cell interior is due to release of Ca^{2+} from perinuclear Ca^{2+} stores. We think that release from intracellular Ca^{2+} stores by a different release mechanism that is insensitive to the drugs we used is also unlikely because the fluorescence changes after five or more depolarizing pulses were less than expected based on simulations with our virtual cell model (see Fig. 3 *C*). This model considers only Ca^{2+} entry through voltage-sensitive Ca^{2+} channels during each pulse and does not include Ca^{2+} release from intracellular Ca^{2+} stores, which would make the expected changes even larger.

To confirm that the increase in the nuclear region occurred progressively during the repetitive stimulation and was not just a transient increase during depolarization, we made a series of measurements (eight measurements in five cells) where the images were captured just before the 10th pulse of a 10-pulse train (i.e., 450 ms after the end of the ninth pulse). The Ca^{2+} distribution in these experiments also showed the typical pattern with the pronounced Ca^{2+} increase in the nuclear region (e.g., Fig. 2 *D*). Moreover, the difference between ''nuclear region'' and ''cytosolic region'' was even more pronounced under these conditions (0.69 ± 0.12, $n = 5$). This suggests that the prominent increase of the signal in the ''nuclear region'' is produced by a gradual process that occurs throughout the train.

Ca^{2+} clearance and decay of Ca^{2+} signals

After stimulation, the Ca^{2+} concentration returns slowly to resting values. To study this decay of intracellular Ca^{2+} after the train, we obtained images at various times after the end of the last depolarizing pulse. Fig. 5 shows an example of such kind of experiment. The distribution of the fluorescence signal is shown in the images in Fig. 5 *A*. It can be seen that the fluorescence signal in all parts of the cell decays slowly

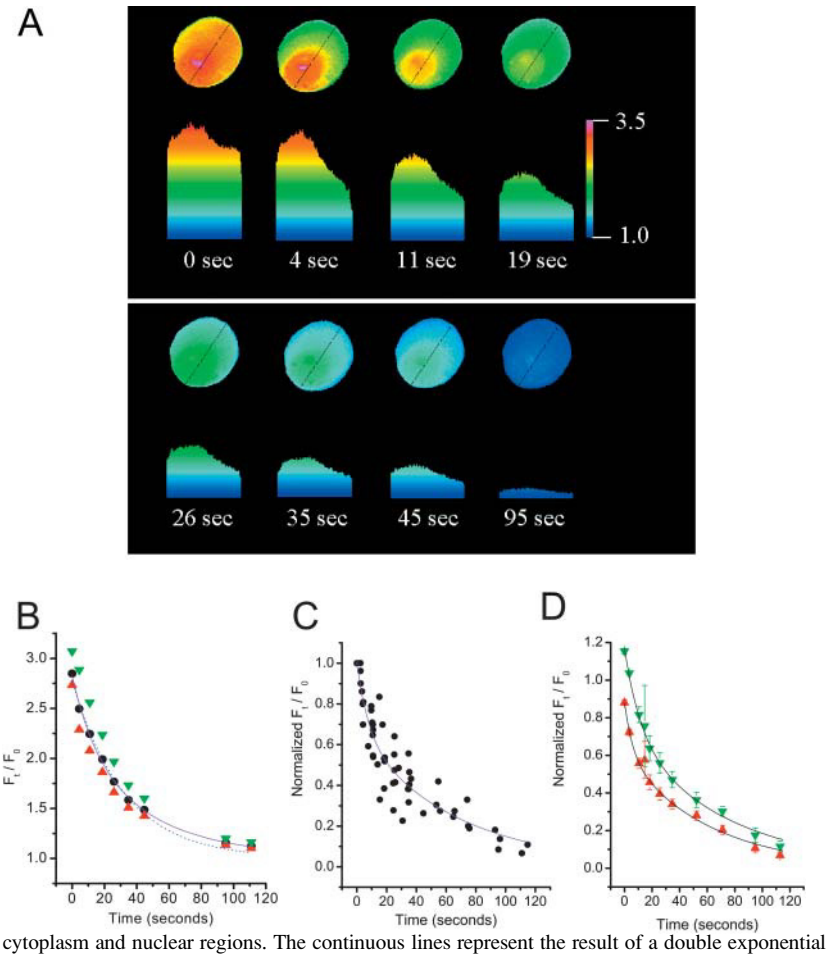

FIGURE 5 Ca^{2+} clearance after stimulation with repetitive depolarizing pulses. Ca^{2+} images were measured after a train of 10 depolarizing pulses (50 ms duration, from −70 to +20 mV, 2 Hz) to investigate the rate of Ca^{2+} clearance. (*A*) Dynamic fluorescence ratios, representing the Ca^{2+} distribution, captured at various times after the end of the 10th pulse. The control image used for all dynamic ratios was captured just before the first depolarizing pulse. (*B*) Analysis of fluorescence changes occurring during Ca^{2+} clearance measured in the same cell as shown in *A*. The spatial averages for the whole cell (*black circles*), the cytoplasm (*red triangles*), and nuclear regions (*green triangles*) are shown. The decay of spatially average values for the whole cell was fitted both to a single exponential equation (*dotted line*) of the type $y = A \cdot e^{-t/\tau}$ ($A = 1.78 \pm 0.04$; $\tau = 32.34 \pm 1.62$; $r = 0.996$; the asymptote was fixed at 1) and to a double exponential equation (*continuous line*) $y = A_1 \cdot e^{-t/\tau_1} + A_2 \cdot e^{-t/\tau_2}$ ($A_1 = 0.73 \pm 0.41$; $\tau_1 = 14.90 \pm 6.38$; $A_2 = 1.10 \pm 0.42$; $\tau_2 = 49.29 \pm 11.70$; $r = 0.999$). The latter avoids the small persistent deviations between the theoretical curve and experimental values seen at the longer times with the single exponential fitting. However, correlation coefficients were very good for both type of equations and we did not find significant differences between them (Fisher test, K. Diem, Scientific Tables, 6th ed, Geigy, Ardsley, NY, 1962). (*C*) Clearance rates obtained from the fitting of the normalized values from spatial averages in series of measurements obtained from six cells. The continuous lines represent the result of a double exponential fitting. The parameters were $A_1 = 0.35 \pm 0.10$, $\tau_1 = 7.74 \pm 3.46$ s, $A_2 = 0.66 \pm 0.10$, $\tau_2 = 67.77 \pm 15.09$ s, $n = 64$, $r = 0.953$; whereas for single exponential fitting, the parameters were $A_1 = 0.94 \pm 0.02$, $\tau = 38.76 \pm 2.69$ ms, $r = 0.9333204$. (*D*) Clearance rates obtained from the fitting of the normalized values from cytoplasm and nuclear regions. The continuous lines represent the result of a double exponential fitting performed on the all the individual data points. For clarity, the figure shows the cytosolic and nuclear experimental results expressed as averages taken from data points binned over 2-s intervals between 0 and 20 s, 10-s intervals between 20 and 40 s, and 20-s intervals between 40 and 120 s. The parameters for the shown curves were, for cytoplasm, $A_1 = 0.27 \pm 0.06$, $\tau_1 = 6.11 \pm 2.50$ s, $A_2 = 0.60 \pm 0.06$, $\tau_2 = 61.50 \pm 9.61$ s, $n = 61$, $r = 0.966$; and for nuclear region, $A_1 = 0.44 \pm 0.22$, $\tau_1 = 11.67 \pm 6.81$ s, $A_2 = 0.73 \pm 0.22$, $\tau_2 = 73.27 \pm 16.45$ s, $n = 61$, $r = 0.947$.

over several minutes, although the differences in fluorescence signal between cytosol and nucleus remain until the signal has almost returned to resting levels. Fig. 5 *B* shows the spatially averaged values of fluorescence signal measured in the whole cell area, cytosolic area, and nuclear area for the cell shown of the experiment represented above. The decay of the nuclear signal is delayed a few seconds with respect to the cytosolic signal, presumably reflecting the fact that the nuclear Ca^{2+} changes are after the cytosolic Ca^{2+} concentration changes. Data pooled from several cells show that during the first 4 s after train stimulation ends, the cytosolic signal decreases significantly compared to the values obtained at the end of the 10th pulse (0.31 ± 0.06, $n = 6$, $p < 0.01$), whereas there was no significant decrease of the nuclear signal during this period (0.15 ± 0.10, $n = 6$).

The decay of spatially average values from the whole cell can be fitted to a single exponential equation of the type $y = A \cdot e^{-t/\tau}$ (Fig. 5 *B*, *dotted line*). On the other hand, an equation with two exponential components $\left(y = A_1 \cdot e^{-t/\tau_1} + A_2 \cdot e^{-t/\tau_2}\right)$ avoids the small persistent deviations between the theoretical curve and experimental values seen with the single exponential fitting, especially at the later times (Fig. 5 *B*, *continuous line*). However, correlation coefficients were very good for both type of equations and we did not find significant differences between them. Fig. 5 *C* shows the decay of the spatially averaged fluorescence using normalized data from six cells, which gave a time constant of 39 ms for a single exponential fit and 8 and 68 ms for a double exponential fit (see legend of Fig. 5 *C* for full details of fitting parameters). Fig. 5 *D* shows the relative time courses of the decay of fluorescence in the cytosolic and nuclear regions after normalizing for the spatially averaged whole cell values at the end of the train stimulus. This data show that the nuclear signal remains higher than the cytosolic signal throughout the recovery to resting Ca^{2+} levels, suggesting that the changes in the nucleus follow from changes in the cytosol.

We also investigated the possibility that mitochondrial Ca^{2+} uptake could modify the pattern of Ca^{2+} removal from the cell. In these experiments ($n = 4$), FCCP and oligomycin

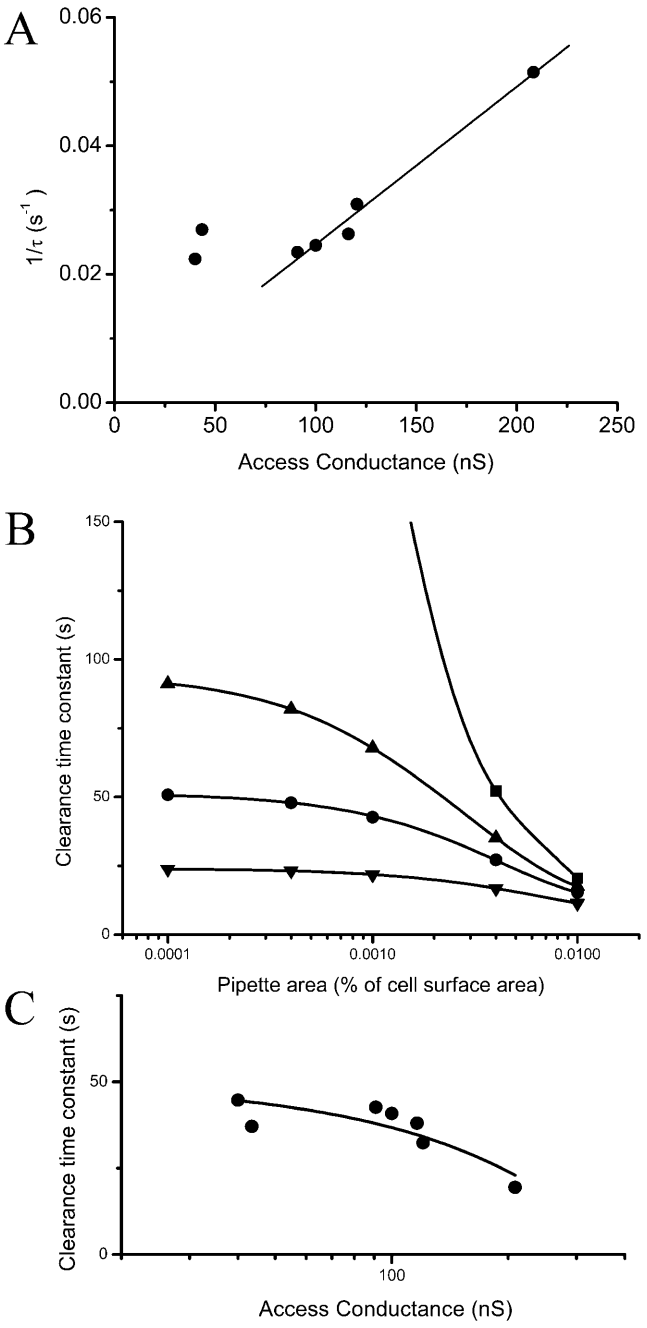

FIGURE 6 Relationship between the Ca^{2+} clearance rate and the access resistance of the patch pipette. (*A*) The clearance time constants were measured from the decay of the spatially averaged fluorescence change after repetitive stimulation (single exponential decays determined as described in Fig. 5). The inverse of these clearance rates was plotted against the access conductance of the patch pipette (G_A) to allow direct comparison with the data of Pusch and Neher (1988). The parameters for the fit of the straight line through the points with $G_A > 90$ nS were: slope $= 0.25 \pm 0.02$ $s^{-1}\cdot M\Omega$, $r = 0.99$. (*B*) The effect of patch pipette access resistance on Ca^{2+} clearance rate was simulated by calculating diffusion into a pipette of different sizes, mimicking different access conductances. The resulting clearance rates were plotted against pipette area (expressed as a percentage of the total cell surface area), which is proportional to the access conductance (G_A). Several curves are shown for different activities of a cellular Ca^{2+} clearance mechanism. In these simulations, we simulated a plasma membrane Ca^{2+}-ATPase with a K_m of 0.83 μM and a V_{max} of variously 0 (*square symbols*), 2 (*triangles*), 4 (*circles*), and 10 (*inverted triangles*) pmol·cm^{-2}·s^{-1}. (*C*) Effect of patch pipette access resistance on measured clearance rate. The time constants of the experimentally derived clearance rates are plotted against the access conductance (inverse of access resistance). Note that the experimental data are closest to the simulations using a V_{max} of 4 pmol·cm^{-2}·s^{-1}, which plateaus at slightly >50 s^{-1}. As the measured clearance rates plateau at slightly <50 s^{-1}, a cellular clearance rate of 5 pmol·cm^{-2}·s^{-1} (not shown) would best describe the experimental measurements of the clearance rate.

were used to inhibit the mitochondrial Ca^{2+} uptake. However, these inhibitors did not lengthen the time constant associated with the decay of the spatially averaged signal after the train ($\tau = 34.26 \pm 1.77$ s). In addition, we studied the effect of Na^+ removal from external and internal solutions to inhibit the participation of plasma membrane Na^+/Ca^{2+} exchange mechanism. This treatment also had no effect on the rate of fluorescence decay after the end of the train ($A = 0.98 \pm 0.03$, $\tau = 43 \pm 0.7$ s, $r = 0.943$, $n = 36$). However, if we consider only the first 8 s after the end of the train, the cytosolic Ca^{2+} signal decays slower when Na^+ is removed (slopes were -0.057 ± 0.005 s^{-1} and -0.030 ± 0.001 s^{-1} for control and zero Na^+, respectively). These experiments suggest that neither Na^+/Ca^{2+} exchange nor mitochondrial Ca^{2+} uptake plays a major role in Ca^{2+} clearance under our experimental conditions, although Na^+/Ca^{2+} exchange may play a minor role.

Our experiments were performed in cells patch-clamped in the whole-cell configuration, where there will be diffusion between the cell and the pipette. To investigate the possible role of diffusional exchange between the cell and pipette, we compared the time constant for Ca^{2+} clearance for individual cells, τ, with the access resistance, which has been shown to control diffusional exchange between the pipette and the cytosol of patch-clamped cells (Pusch and Neher, 1988). A plot of $1/\tau$ against the access conductance G_A is shown in Fig. 6 *A*. Pusch and Neher (1988) have previously shown that diffusion between a cell and a patch pipette yields a linear plot of $1/\tau$ vs. G_A for many water-soluble molecules, including fluorescent Ca^{2+} indicators. There is a good linear fit (slope $= 0.25 \pm 0.02$ $s^{-1}\cdot M\Omega$, $r > 0.99$) between $1/\tau$ and G_A when the conductance is larger than 90 nS, but for higher resistances (>10 MΩ), the clearance rate deviates from the linear relationship. This suggests that in most of our regular whole-cell conditions, the main mechanism of Ca^{2+} removal from cytosol after the large gradients close to the membrane have dissipated is passive diffusion into the patch pipette, and that it is only when the access resistance is high that the physiological cellular mechanisms predominate.

To analyze the relative role of diffusional exchange with the patch pipette and cellular clearance mechanisms, we did a number of computer simulations where we changed the pipette tip size (to mimic changing the access resistance) and V_{max} of a plasma membrane clearance mechanism (nominally we used the Ca^{2+}-ATPase, but Na^+/Ca^{2+} exchange

would behave similarly) and calculated the clearance time constant for the average cellular fluorescence change. Fig. 6 *B* shows plots of the clearance rate against pipette size, expressed as a percentage of the cell surface area. The diffusion is simulated as a two-compartment model, the pipette and the outer 100 nm cytosolic shell in the radial diffusion model. As the clearance is slow, we assume that the outer shell is at spatial equilibrium (in effect, we assume that the diffusion across a pipette tip of a size that is a fraction of the cell surface area is equivalent to diffusion distributed over the entire cell surface with a fractional permeability). In the absence of a cellular Ca^{2+} uptake mechanism, the clearance time rises dramatically as the pipette size (access conductance) decreases (Fig. 6 *B*, *squares*). In the presence of various activities of Ca^{2+}-ATPase, the clearance rate plateaus at a rate determined by the V_{max} of the clearance mechanism (Fig. 6 *B*). Fig. 6 *C* shows the measured clearance rates replotted against the series conductance. This plot is analogous to Fig. 6 *B*, but uses the experimental parameter, the access conductance, instead of the simulation parameter, the pipette area as a percentage of the cell surface. As this data seem to asymptote to a clearance rate of ~40 s, which corresponds to simulations using a Ca^{2+}-ATPase with a V_{max} of 5 pmol·cm^{-2}·s^{-1} (Fig. 6 *B*) and a K_m of 0.83 μM (Nowycky and Pinter, 1993), we used this value of the V_{max} for the physiological clearance mechanism for future simulations. We also used a fractional area of 0.004% of the cell surface to simulate a typical access resistance of ~10 MΩ

Simulation of Ca^{2+} gradients during and after repetitive stimuli

One of the goals of this study is to develop a ''virtual cell'' describing dynamic and spatial aspects of Ca^{2+} signaling in adrenal chromaffin cells. Our original reason was to use this to investigate the Ca^{2+}-dependent regulation of depolarization-induced exocytosis, but the model will also be used to investigate potential mechanisms for the larger fluorescence increases in the nuclear region (see later). We want to use the experimental data on the time course and spatial distribution of the Ca^{2+} increases after depolarizing stimuli to develop a computer model that accurately reproduces the physiological responses. We have previously developed a radial diffusion model that describes the development and dissipation of Ca^{2+} gradients in response to short depolarizing pulses (Marengo and Monck, 2000). This model accounts for the distribution of the Ca^{2+} entering through voltage-activated Ca^{2+} channels by diffusion and binding to endogenous and exogenous Ca^{2+} buffers. Here we extend the model to take account of the Ca^{2+} distribution during repetitive stimulation. In Fig. 3 *C*, the average values for the whole cell are superimposed over a simulation of the pattern of Ca^{2+} gradients, using the parameters determined to best reproduce the pattern of Ca^{2+} gradients during development and dissipation during and after a single depolarizing pulse (Marengo and Monck, 2000). Although the averages match the simulation well for the first four or five depolarizing pulses, the simulation significantly overestimates the fluorescence changes for seven or more pulses. These results suggest that a more complete model must account for additional mechanisms limiting the total increase in fluorescence. One possible mechanism is Ca^{2+} channel rundown, which usually occurs during a train stimulus. Some Ca^{2+} channel rundown is apparent in Fig1 *B*, although the extent is less than average in these cells. In our experiments, the Ca^{2+} current is reduced to 88.6 ± 1.33% ($n = 15$) of the initial value after five pulses and to 74.0 ± 2.1% after 10 pulses. We have simulated the rundown empirically, as described in Methods, but the reduced Ca^{2+} influx is insufficient to account for the smaller fluorescent changes after 7–10 pulses (data not shown). Other mechanisms that could reduce the fluorescence changes during repetitive stimulation are the Ca^{2+} clearance mechanisms for restoring resting Ca^{2+} levels, which, as discussed in the last section, involves mainly diffusional exchange with the pipette under our experimental conditions. The pipette Ca^{2+} clearance is included in the simulation shown in Fig. 7 *A*, but is also insufficient to account for the fluorescence changes observed. We found that the best way of reducing the Ca^{2+} changes was to use an endogenous Ca^{2+} buffer with four binding sites and introduce positive cooperativity for the fourth Ca^{2+} bound (see Fig. 7, *B* and *C*). The rationale for this was that most EF-hand Ca^{2+} binding proteins have four Ca^{2+} binding sites, and cooperativity has been observed in several cases (Iida, 1988; Leathers et al., 1990; Morimoto and Ohtsuki, 1994; Olwin and Storm, 1985; Teleman et al., 1983). However, we stress that these changes were introduced so that our simulations better reproduced the measured fluorescence changes in the cytosol and not because we have any experimental evidence that the endogenous Ca^{2+} binding protein in adrenal chromaffin cells has four Ca^{2+} binding sites or exhibits positive cooperativity.

We used the computer simulations of the expected fluorescence changes as a tool to explore putative mechanisms to account for the larger fluorescence increase in the nuclear region. As shown earlier, comparison of the fluorescent images mapping the Ca^{2+} distribution with bright-field images showed that the large fluorescence increase inside the cell colocalized with the nucleus. We also showed pharmacological evidence indicating that Ca^{2+} release from perinuclear Ca^{2+} stores was unlikely to be involved. An alternative explanation is that this larger internal increase occurs due to the presence of a distinct nuclear compartment. To investigate this possibility, we considered several different mathematical models to explain the spatial distribution of the measured fluorescence changes, notably the delayed increase and the large increases at the end of the train. Fig. 7 shows simulations of the

fluorescence changes obtained with three types of potential mechanisms that were able to successfully simulate the observed experimental results: one involving active nuclear Ca^{2+} transport mechanisms, the second using a passive mechanism involving diffusion and accumulation of bound Ca^{2+}-indicator complex in the nucleus, and the third mechanism with different fluorescence properties of the Ca^{2+} indicator in the nucleus.

Fig. 7 *A* shows a simulation performed using the modified radial diffusion model of a cell with a nucleus placed in the center of the cell. The nucleus was given active Ca^{2+} transport mechanisms for uptake and efflux, both with first-order dependence on Ca^{2+}. Here we used a V_{max} of 50 pmol·cm^{-2}·s^{-1} for both Ca^{2+} uptake and efflux and a K_m of 0.2 μM and 0.75 μM, respectively. To simulate our experimental conditions, we included 0.3 mM rhod-2 and 0.2 mM EGTA as exogenous mobile Ca^{2+} buffers that are introduced through the patch pipette, and assumed an endogenous immobile buffer with the properties previously estimated (0.968 mM concentration with $K_d = 1$ μM, $k_{on} =$ 50 m M^{-1}·ms^{-1}, and $k_{on} = 0.05$ms^{-1} to give a buffer capacity of 800). These were the conditions established in our previous study (Marengo and Monck, 2000) and used in the simulation shown in Fig. 3 *C*. The nucleus was given 1% of the endogenous cytosolic Ca^{2+} buffer concentration. The rationale for the lower buffer capacity is that the Ca^{2+} binding proteins that are candidate Ca^{2+} buffers are mainly cytosolic proteins (Burgoyne and Geisow, 1989; Heizmann, 1992). The value used is not critical, as when using 10% for the nuclear Ca^{2+} buffer, the nuclear fluorescence and Ca^{2+} changes were suppressed by <5% relative to Fig. 7 *A* (data not shown). However, similar quantitative results can be obtained with higher or lower nuclear buffer by changing the capacities of the Ca^{2+} transport mechanisms.

The time course of the fluorescence changes simulated with the model (Fig. 7 *A*) shows many features of the measured fluorescence changes observed during a train of depolarizing pulses. Early on there are prominent submembrane gradients with the increase in the nucleus lagging behind. Then there is the progressively increasing cytosolic signal, and finally the appearance of a larger nuclear increase. The ''blurred'' fluorescence profiles (Fig. 7 *A*, *right*) show that an increase in the nucleus, which appears as an abrupt step increase with respect to the cytosol in the simulated profiles (Fig. 7 *A*, *middle*), would be observed as a smooth increase slightly larger than the cytosol due to the blurring effect of the microscope optics.

The second type of mechanism involves passive diffusion of Ca^{2+} and indicator into the nucleus. Restricted diffusion of Ca^{2+} and indicator across the nucleus envelope provides the delayed fluorescence increase, and accumulation of the Ca^{2+}-indicator complex in the nucleus accounts for the larger fluorescence increase seen late in the train. Fig. 7 *B* shows a model simulation where the latter is achieved by assuming that the Ca^{2+}-indicator complex binds to intranuclear constituents more than the free form of the indicator. Other studies have indicated that substantial fractions of the Ca^{2+} indicator may be bound to intracellular constituents, particularly in skeletal muscle myoplasm (Baylor and Hollingworth, 1988; Harkins et al., 1993; Konishi et al., 1988), although we know of no specific reports for indicator binding in the nucleus. This model is similar to that shown in Fig. 7 *A*, except that the passive model for the nuclear Ca^{2+} and indicator distribution is used instead of a mechanism involving active Ca^{2+} transport. Here we assume that the nucleus is permeable to Ca^{2+} and mobile buffers to an extent that movement is restricted to 0.2% of that occurring by diffusion without the nuclear membrane, consistent with what we might expect for diffusion through the nuclear pores. In this simulation, ~50% of the Ca^{2+}-indicator complex is bound, whereas <1% of the free indicator is bound. The result is net accumulation of the Ca^{2+}-indicator complex and a larger fluorescence increase in the nucleus.

A third possible explanation for the larger fluorescence increase in the nucleus, which also involves passive movement of Ca^{2+} and indicator across the nuclear envelope, is shown in Fig. 7 *C*. Here we assume that the fluorescence properties of the Ca^{2+} indicator are different in the nucleus, so that the fluorescence of the Ca^{2+}-bound indicator is increased (i.e., F_{max}/F_{min}, the ratio of the Ca^{2+}-saturated and free indicator, is increased in the nucleus). This phenomenon has been reported for the Ca^{2+} indicator fluo-4 (Thomas et al., 2000). To reproduce the delay before the large nuclear increase was observed, we also had to assume that the nucleus was partially permeable to Ca^{2+}, EGTA, and indicator. As before, we assumed that the permeability allowed diffusion at 0.2% of the rate that occurred for diffusion in the cytosol. Unlike the previous two mechanisms, the larger fluorescence increase is not due to a higher Ca^{2+} concentration in the nucleus, but is solely due to the properties of the indicator fluorescence.

We also used computer simulations to consider a number of other potential mechanisms that we thought might be able to explain the difference in the fluorescence changes observed in the cytosol and nucleus. Mechanisms tested included models involving differences in accessible volume in the cytosol and nucleus, differences in the assumed resting Ca^{2+} concentration in the cytosol and nucleus, differences in diffusion coefficient of Ca^{2+} and/or mobile buffers, differences in affinity or buffer capacity of endogenous buffer in cytosol and nucleus, and differences in the K_d of the Ca^{2+} indicator. However, we were unable to adequately reproduce the observed experimental results with any of these mechanisms. We have only shown the three types of mechanism that were able to reasonably reproduce the relative fluorescence changes in the cytosol and nucleus. The relative merits of these mechanisms as possible explanations for the larger fluorescence increase in the nucleus will be discussed later (see Discussion).

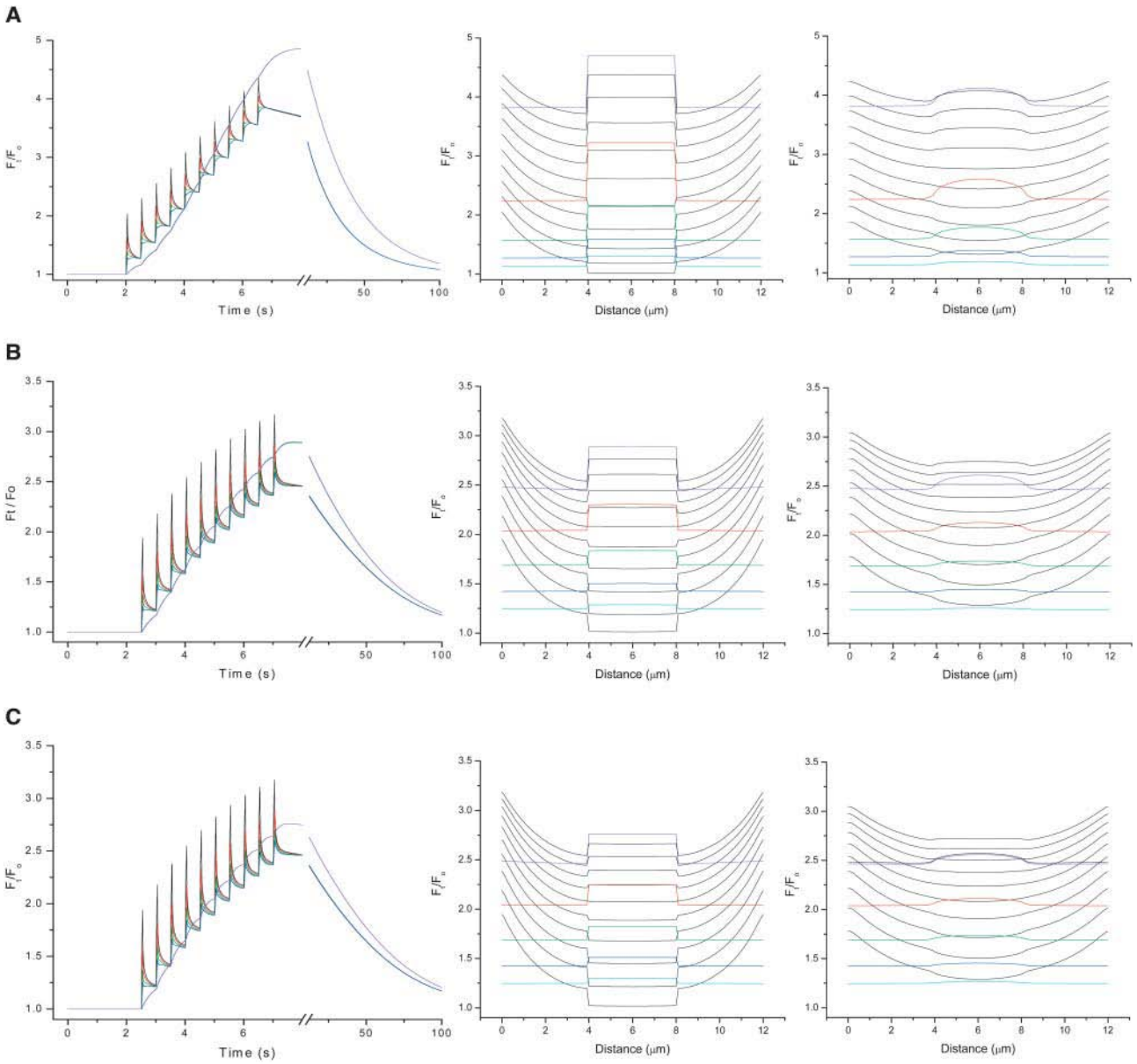

FIGURE 7 Simulation of dynamics of Ca^{2+} gradients during repetitive stimuli. A virtual cell describing the pattern of Ca^{2+} distribution after stimulation with repetitive depolarizing stimuli was used to simulate fluorescence and Ca^{2+} distributions under experimental protocols similar to those used for the measurements in Figs. 1 and 5. This model extends the model of Marengo and Monck (2000) by introducing three new features: Ca^{2+} channel inactivation (see Methods), Ca^{2+} clearance by the patch pipette (see Methods and Fig. 6), and a centrally located nucleus. Three different mechanisms were used to try and replicate the experimentally observed results. (*A*) The nucleus was given active Ca^{2+} transport mechanisms for uptake and efflux, both with first-order dependence on Ca^{2+}. Here we used a V_{max} of 50 pmol·cm^{-2}·s^{-1} for both Ca^{2+} uptake and efflux and a K_m of 0.2 μM and 0.75 μM, respectively. To simulate our experimental conditions, we included 0.3 mM rhod-2 and 0.2 mM EGTA as exogenous mobile Ca^{2+} buffers that are introduced through the patch pipette, and assumed an endogenous immobile buffer with the properties previously estimated (0.968 mM concentration with $K_d = 1$ μM, $k_{on} = 50$m M^{-1}·ms^{-1} and $k_{on} = 0.05$ ms^{-1} to give a buffer capacity of 800). The nucleus was given 1% of the cytosolic Ca^{2+} buffer concentration. (*Left*) Time course of simulated changes in fluorescence (expressed as F_t/F_o). The different lines represent the time courses in the outer 100 nm shell and shells 1, 2, 3 (cytosolic), 4, 5, and 6 (nuclear) μm from the cell membrane. (*Middle*) Profiles of simulated fluorescence gradients taken after each pulse (*black lines*) and at 20-s intervals thereafter (*colored lines*). (*Right*) Profiles of simulated fluorescence gradients after accounting for the blurring effect of out-of-focus light introduced by the imaging optics. (*B*) Simulation using a model with a passive mechanism for the nuclear Ca^{2+} distribution is used instead of an active mechanism. Here we assume that the nucleus is permeable to Ca^{2+} and mobile buffers to an extent that movement is restricted to 0.2% of that occurring by diffusion without the nuclear membrane. To get the gradient in the nucleus, we assume that the Ca^{2+}-rhod-2 complex binds to nuclear constituents resulting in net accumulation of indicator. In this simulation, 53% of the Ca^{2+}-indicator complex and 0.5% of the free indicator are bound to nuclear sites at steady state. In these simulations, the endogenous buffer in the cytosol was given four binding sites and positive cooperativity introduced for binding of the fourth Ca^{2+} ion, as described in Methods. This positive cooperativity increases the buffer capacity at higher Ca^{2+} concentrations, which explains the smaller changes later in the train of pulses in *B* and *C* (compared to *A*). (*C*) Simulation using a model with a mechanism where the fluorescence difference between the cytosol and the nucleus was generated by

Effect of ionomycin

Fig. 8 shows an experiment where the Ca^{2+} ionophore ionomycin was used to elevate the Ca^{2+} concentration. The ionomycin caused a slow fluorescence increase over 3–10 min (Fig. 8 *A*) and, as with electrical stimulation, there was a larger fluorescence increase in the nucleus (4.3 ± 0.4 compared to 3.1 ± 0.3, $n = 6$). The ionomycin treatment gives a larger relative increase in the nucleus (1.38 ± 0.01, $n = 6$) than electrical stimulation (1.15 ± 0.02, $n = 19$). As the ionomycin experiments were over longer time spans, the larger F_t/F_o change in the nucleus after ionomycin treatment may be due to slow accumulation of Ca^{2+}-indicator complex in the nucleus due to binding, as illustrated by the simulation shown in Fig. 8 *B* using the same model as described for Fig. 7 *B*. This simulation also reproduces the larger relative increase in the nucleus with ionomycin than with electrical stimulation (compare Fig. 8 *B* with Fig. 7 *B*). Alternatively, the measured results can also be reproduced by a simulation using the model described for Fig. 7 *C* where the fluorescence properties of indicator are different in the nucleus (Fig. 8 *C*).

DISCUSSION

In this study we have investigated the spatial organization of the Ca^{2+} signal in electrically stimulated adrenal chromaffin cells. We have used pulsed laser Ca^{2+} imaging to measure the dynamics of Ca^{2+} gradients in response to repetitive depolarizing stimuli. A major goal of this study was to develop a virtual cell model to simulate the spatial distribution of the measured Ca^{2+} changes. We were able to identify three spatially localized Ca^{2+} signals with different dynamic properties: a Ca^{2+} gradient beneath the plasma membrane that develops and dissipates relatively rapidly; an increase in the cytosol that shows step increments with successive stimuli; and a slower increase in nucleus that develops after a delay. Here we discuss the evidence for these conclusions, possible mechanisms, and physiological consequences.

Ca^{2+} signals during repetitive stimulation of adrenal chromaffin cells

Short single depolarizations (10–100 ms) lead to the development of submembrane Ca^{2+} gradients, which dissipate to leave a homogenously elevated cytoplasmic Ca^{2+} concentration. The gradient dissipation comprises a fast phase (tens of milliseconds), mainly due to diffusion, and a slow phase (hundreds of milliseconds), mainly due to slow release of Ca^{2+} from intracellular Ca^{2+} buffers (Marengo and Monck, 2000). The homogenously elevated Ca^{2+} decays to rest relatively slowly (see later for discussion of clearance mechanism). Under these conditions, we can clearly distinguish a fast localized Ca^{2+} signal beneath cell membrane and a slower ''global'' cytosolic Ca^{2+} signal that persists for seconds.

Stimulation with repetitive stimuli, which might better represent the physiological signal, reveals a different pattern of Ca^{2+} signals. A second, third, or fourth stimulus results in a Ca^{2+} gradient, similar to that after the first pulse, on top of the homogenously elevated ''residual'' Ca^{2+} that remains after dissipation of the previous gradient. As the number of pulses increases, a larger fluorescence increase in a region near the center of the cell becomes visible and is prominent after 7–10 pulses. At intermediate times the results were variable, with an edge-to-center gradient still clear in some cells (e.g., Fig. 1), and a larger increase in the cell interior in other cells. After 10 pulses, the fluorescence increase in the center of the cell was usually larger than that measured at the cell periphery, and was typically 2–4 times higher than the maximum values obtained for fluorescence gradients at the end of single pulses (Fig. 1).

The large Ca^{2+} increase occurs near the center of the cell, but not at the geometric center. Comparison of the fluorescent images mapping the Ca^{2+} distribution with bright-field images showed that the large fluorescence increase in the cell interior colocalized with the nucleus (Fig. 2). Analysis of the fluorescence changes in the cytosolic and nuclear regions from several cells shows that the nuclear signal lags behind the cytosolic signal for the first five pulses and the then becomes larger thereafter (Fig. 3 *A*).

One possible explanation for the large fluorescence increase in the vicinity of the nucleus is that there is release of Ca^{2+} from intracellular stores in the perinuclear region. The nucleus is surrounded with endoplasmic reticulum, which serves as intracellular Ca^{2+} stores (Burgoyne et al., 1989; O'Sullivan et al., 1989). In addition, IP_3 induced release of Ca^{2+} from the nuclear envelope has been reported (Gerasimenko et al., 1995; Stehno-Bittel et al., 1995). Thus it is possible that Ca^{2+} release from such stores might contribute to the large Ca^{2+} increase in the cell interior. The presence of out-of-focus light, due to the optical limits of fluorescent microscopy, means that we cannot definitively distinguish between colocalization with the nucleus and colocalization with, for example, perinuclear endoplasmic reticulum or the nuclear envelope. To investigate this possibility, we performed some pharmacological experiments to inhibit or empty such Ca^{2+} stores. However, the pattern of Ca^{2+} gradient was not modified by inhibition of

assuming different properties of the indicator in the nucleus. In this case, the F_{max}/F_{min} was five times larger in the nucleus. Increasing this ratio did not increase the difference between the cytosol and nucleus. As in the simulation shown in *B*, the nucleus permeability to Ca^{2+} and mobile buffers is 0.2% of that occurring by free diffusion, the cytosolic Ca^{2+} buffer was given four binding sites, and positive cooperativity for binding the fourth Ca^{2+} ion.

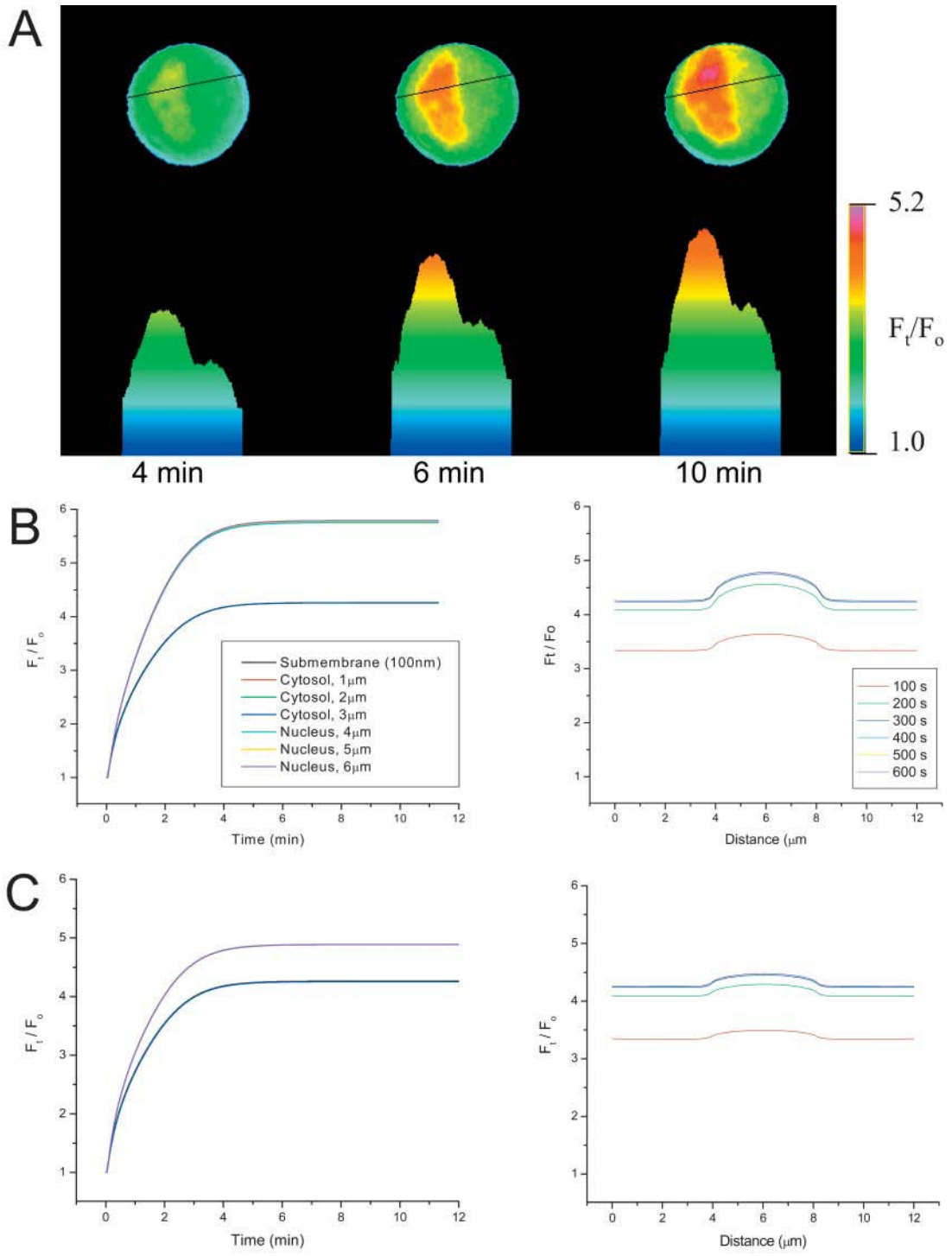

FIGURE 8 Effect of ionomycin on the distribution of Ca^{2+} indicator fluorescence. The Ca^{2+} ionophore, ionomycin (10 μM), was added to the extracellular medium, and images taken before and at various times afterward. (*A*) F_t/F_o images calculated from the images taken 4, 6, and 10 min after ionomycin addition, using the image taken before ionomycin addition as the reference (F_o). The profiles through the nucleus along the line indicated are shown beneath. (*B*) (*Left*) Simulation of fluorescence time course using the model described for Fig. 7 *B*, where the higher nuclear fluorescence is due to accumulation of bound Ca^{2+}-indicator complex. In these simulations, the plasma membrane was made permeable to Ca^{2+} by setting the permeability factor to 0.00015 (see Methods). Note that the changes in the cytosol and nucleus are almost uniform so the lines superimpose for the cytosolic shells (0, 10, 20, and 30 (*blue*)) and the nuclear shells (40, 50, and 60 (*magenta*)). (*Right*) Profiles of simulated fluorescence gradients at 100-s intervals after addition of ionomycin. The profiles were blurred to mimic the effect of out-of-focus light introduced by the imaging optics. (*C*) (*Left*) Simulation of fluorescence time course using the model described for Fig. 7 *C*, where the higher nuclear fluorescence is due to the fluorescence properties of the Ca^{2+} indicator. (*Right*) Blurred profiles of simulated fluorescence gradients at 100-s intervals after addition of ionomycin.

Ca^{2+}-induced Ca^{2+} release with ryanodine, inhibition of IP_3-induced Ca^{2+} release with xestospongin, or depletion of intracellular Ca^{2+} stores with thapsigargin, as shown in Fig. 4. In addition, inhibition of mitochondria had no effect. Thus, release of Ca^{2+} from perinuclear Ca^{2+} stores is unlikely to explain the larger fluorescence increase in the vicinity of the nucleus. Furthermore, the measured spatially averaged Ca^{2+} changes after 5–10 pulses were smaller than expected based on predictions with our diffusional model (Fig. 3 *C*), which argues against an additional source of Ca^{2+} entering the cytosol. Other possible explanations for the observation that the change in nuclear fluorescence becomes larger than the change in cytosolic fluorescence will be discussed later.

Ca^{2+} clearance mechanisms in patch-clamped cells

After the formation of Ca^{2+} gradients, the gradients dissipate to leave a homogenously elevated cytosolic Ca^{2+} concentration (see (Marengo and Monck, 2000)). This elevated Ca^{2+} slowly returns to resting levels (Fig. 5). The most important Ca^{2+} clearance mechanism under our experimental conditions is usually diffusional exchange of Ca^{2+} and Ca^{2+} complexes with mobile buffers in the cytosol with the solution in the patch pipette. As shown in Fig. 6 *A*, our measured time constant for Ca^{2+} clearance from the cytosol is inversely proportional to access conductance (G_A). A previous study of the rate of diffusional exchange between the cytosol of small cells and patch pipettes, which measured diffusion of fluorescent molecules into patch-clamped adrenal chromaffin cells, found that the inverse of the diffusion time constant ($1/\tau$) was proportional to the access conductance with a proportionality constant that was determined by the diffusion coefficient and size of the diffusing molecule (Pusch and Neher, 1988). This relationship can be used to estimate the diffusion constant in our experiments. Since most of the Ca^{2+} is bound to endogenous and exogenous Ca^{2+} buffers, the main diffusing species will be the Ca^{2+} complexes with the mobile Ca^{2+} buffers, which are rhod-2 and EGTA in our whole-cell experiments. According to this study by Pusch and Neher (1988), the diffusion coefficient, $D = (78.4 \pm 6.6)/(\tau G_A)$. Using the data in Fig. 6 from the five cells that fit the linear relationship, we estimate a diffusion coefficient of 120 $\mu m^2/s^{-1}$, after correcting for cell size according to the equations given by Pusch and Neher (1988). This diffusion coefficient is in reasonably good agreement with the 100 $\mu m^2/s^{-1}$ that we use in our simulations.

In some experiments, when the access resistance is high, the measured clearance rate is faster than predicted by the theory just described. The slowest clearance rates have time constants of ~40−50 s. We attribute this Ca^{2+} clearance to physiological mechanisms. It is difficult to study the physiological Ca^{2+} clearance mechanism under our experimental conditions, because the pipette resistance dominates Ca^{2+} clearance in most of our experiments. Increasing the pipette resistance is not practical as then we don't get good diffusional exchange of the Ca^{2+} indicator, which is necessary for the Ca^{2+} measurements. In addition, our experiments generally involve small stimuli under strongly buffered conditions, so the measured Ca^{2+} changes are relatively small. Other studies using stronger stimulating protocols have variously implicated a role for plasma membrane Na^+/Ca^{2+} exchange and mitochondrial mechanisms (Herrington et al., 1996; Pan and Kao, 1997; Tang et al., 2000). This is not inconsistent with our experiments. As described in Results, there is a slight slowing of clearance immediately after stimulation when extracellular Na^+ is removed suggesting that Na^+/Ca^{2+} exchange may participate as the endogenous clearance mechanism in our experiments. Nevertheless, diffusional exchange with the patch pipette appears to be an important clearance mechanism under our experimental conditions.

A virtual cell to explain dynamic Ca^{2+} redistributions during repetitive stimulation

Our previous working model for simulation of Ca^{2+} gradients was designed to reproduce the development and dissipation of the Ca^{2+} gradients during and after single depolarizing pulses (Marengo and Monck, 2000). However, when we compared the measured spatially averaged fluorescence changes during repetitive stimuli with the values predicted by these simulations, we found that the measured fluorescence changes after five or more pulses were smaller than expected. The reduction in the changes is unlikely to be due to indicator saturation, since larger fluorescence changes were seen in the ionomycin experiments (Fig. 8). We incorporated several new features into our model to try to account for this observation. First, we included Ca^{2+} channel rundown (see currents in Fig. 1), although this alone had only a small effect (data not shown). Second, we have incorporated diffusional exchange with the pipette as the major clearance mechanism responsible for restoring elevated Ca^{2+} concentrations to resting levels. As just discussed, at higher access resistances there seems to be a minimum clearance rate of ~40–50 s, which we attribute to endogenous mechanisms. A comparison of simulations with experimental values suggested an appropriate endogenous rate for our model (Fig. 6). Thus we increased the V_{max} of the Ca^{2+}-ATPase from 2 to 5 $pmol \cdot cm^{-2} \cdot s^{-1}$. This change was also made by Klingauf and Neher (1997) to fit their measured Ca^{2+} clearance rates. Although we have implemented the endogenous Ca^{2+} clearance mechanism as a Ca^{2+}-ATPase, we do this for historical reasons (see Klingauf and Neher, 1997; Marengo and Monck, 2000; Nowycky and Pinter, 1993), and the first-order process that we simulate could equally well represent the Na^+/Ca^{2+} exchanger.

Even after including Ca^{2+} channel rundown and Ca^{2+} clearance, the measured fluorescence changes were still smaller than the simulated changes late in the train of depolarizing pulses (see Fig. 7 *A*). This suggests that there may be additional buffering at higher Ca^{2+} levels. We found no effect of agents that inhibits or prevents Ca^{2+} accumulation into intracellular stores, which might act as active Ca^{2+} buffers. This raises the possibility that the increased buffering is a property of the endogenous Ca^{2+} buffer(s). Since most EF-hand Ca^{2+} binding proteins have four Ca^{2+} binding sites and cooperativity has been observed in several cases, including troponin-C (Iida, 1988; Morimoto and Ohtsuki, 1994; Teleman et al., 1983), calmodulin (Olwin and Storm, 1985), and calbindin (Leathers et al., 1990), we thought that positive cooperativity might achieve the observed result. For the simulations shown in Fig. 7, *B* and *C*, we modified the properties of the endogenous buffer to include four Ca^{2+} binding sites (while keeping the total number of binding sites constant) and increased the affinity for binding of the fourth Ca^{2+} ion. Other properties of the endogenous buffer were kept constant. Although these changes were made for empirical reasons, as we have no direct evidence that the endogenous Ca^{2+} binding protein in adrenal chromaffin cells has four Ca^{2+} binding sites or exhibits positive cooperativity, using an endogenous buffer with these properties achieved the desired aim and produced simulations that better reproduced the measured changes in F_t/F_o (see Fig. 3 *A*).

Finally, we must incorporate some mechanism to explain the large fluorescence increase in cell interior. As discussed above, we believe this is a Ca^{2+} increase in the nuclear compartment and not due to intracellular release from perinuclear stores. We decided to explore several mechanisms to reproduce the measured pattern of fluorescence distribution in the cytosol and nucleus using mathematical modeling. The model must be able to explain the following properties of the measured Ca^{2+} distribution: First, the model must be capable of explaining a large nuclear increase after seven or more pulses. Second, the time course of the nuclear increase must initially lag behind the cytosol for the first 1–3 pulses (see Fig. 3). Although it is difficult to see in the images because of out-of-focus light, we can sometimes see that the nuclear fluorescence is smaller than the surrounding cytosol by the presence of a small inflection in the fluorescence gradient at the edge of the nucleus (data not shown). Third, the model must show that the difference between the nucleus and the cytosol is larger before the 10th pulse than immediately after. And finally, the difference between the nucleus and cytosol should be maintained for tens of seconds after the end of the train (Fig. 5).

Nuclear Ca^{2+} signals generated by active nuclear Ca^{2+} transport mechanisms

A number of previous studies have suggested that the nuclear Ca^{2+} may be regulated distinctly from the cytosolic Ca^{2+} concentration (e.g., al-Mohanna et al., 1994; Williams et al., 1985). The original study using fura-2 in smooth muscle cells showed a nuclear increase that was larger than the cytosolic Ca^{2+} concentration change (Williams et al., 1985), whereas al-Mohanna et al. (1994) showed that the nucleus guarded against large Ca^{2+} changes. Perhaps more surprising was the observation that isolated nuclei were able to regulate their internal Ca^{2+} concentration, possibly using Ca^{2+} pumps to transport Ca^{2+} from the extranuclear space (Nicotera et al., 1989).

We considered whether an active nuclear Ca^{2+} transport mechanism could explain the large nuclear fluorescence we observed during repetitive stimulation. We simulated active Ca^{2+} uptake into the nucleus as a first-order process dependent on Ca^{2+} (see Methods). In this model we assumed a lower nuclear Ca^{2+} buffering capacity, as most Ca^{2+} binding proteins are thought to be cytosolic (Burgoyne and Geisow, 1989; Heizmann, 1992). This assumption was not necessary, as higher nuclear buffer capacities could have been accommodated by increasing the V_{max} of the Ca^{2+} uptake mechanism. Such an active Ca^{2+} uptake mechanism was able to reproduce the fluorescence increase during the stimulation (Fig. 7 *A*). However, to explain the clearance of the Ca^{2+} signal after the stimulation, we needed to include an active efflux mechanism, also with a first-order dependence, but with a lower affinity (see Fig. 7 *A*). We also tried using a passive leak for efflux, but the leak was never able to bring the Ca^{2+} concentration down after the stimulation, as the Ca^{2+} uptake was always greater. We could have invoked an inactivation of the Ca^{2+} uptake mechanism, but thought it simpler to use an active uptake and efflux mechanism.

The ability of the nucleus to actively take up Ca^{2+} was proposed when it was found that isolated nuclei appeared to regulate the intranuclear Ca^{2+} concentration at different levels from the surrounding media (Nicotera et al., 1989). However, this conclusion has been challenged by a study showing that the Ca^{2+} indicator accumulates into the nuclear envelope and not into the intranuclear space (Gerasimenko et al., 1995). In these studies, the indicator was loaded as the acetoxymethyl ester form, which is membrane permeable and was able to get into the nuclear envelope. As a result, the fluorescence measurements were detecting Ca^{2+} accumulation into the nuclear envelope, not the nuclear space (Gerasimenko et al., 1995, 1996). Thus, although the mechanism of Ca^{2+} transport into the nucleus is still debated, it seems most likely that the nucleus is partially permeable to Ca^{2+}, and that Ca^{2+} probably enters the nuclear space through the nuclear pore (see Gerasimenko et al., 1995, 1996). However, although we are unaware of any direct experimental evidence suggesting that the nucleus has unique active uptake and efflux mechanisms, our model clearly demonstrates the feasibility of such an active mechanism, and the results are consistent with our experimental data.

Nuclear Ca^{2+} signals generated by passive Ca^{2+} and indicator redistribution

We have spent considerable effort considering passive mechanisms by which the large increase in the nucleus is not due to active transport of Ca^{2+}, but instead is due to passive diffusion of Ca^{2+} and mobile Ca^{2+} buffers. All such mechanisms assume a restricted permeability of Ca^{2+} and Ca^{2+} indicator into the nucleus, but that the final resting (steady-state) distribution is due to diffusional equilibrium across the nuclear membrane. We should note here that in our experiments, we loaded the cells with the membrane impermeant acid form of the indicator by dialysis from the patch pipette, so it is unlikely that the Ca^{2+} indicator is in the endoplasmic reticulum or nuclear envelope in our experiments, as can occur with ester loading (Gerasimenko et al., 1995).

One plausible passive mechanism would be if the Ca^{2+}-bound form of the indicator bound to intranuclear constituents, which results in net accumulation of indicator when the Ca^{2+} is elevated. There are several reports of Ca^{2+} indicator diffusion being restricted inside cells (Gabso et al., 1997; Konishi et al., 1988), as well as measurements of indicator binding to intracellular constituents in skeletal muscle myoplasm (Baylor and Hollingworth, 1988; Harkins et al., 1993), although we know of no reports for binding specifically in the nucleus. A simulation based on such a model is shown in Fig. 7 *B*. The nuclear fluorescence increase would initially lag behind the cytosolic increase due to restricted permeability into the nucleus and then would gradually increase as Ca^{2+}-rhod-2 diffused into the nucleus. In this case, the fluorescence ratio increase would be partially due to a dynamic change in indicator concentration. However, as shown in Fig. 9 *A*, the Ca^{2+} concentration is also raised above cytosolic values. The explanation is that Ca^{2+} is carried into the nucleus as the Ca^{2+}-indicator complex and is ''trapped'' there because the equilibrium with the bound indicator is relatively fast compared to diffusion of Ca^{2+} out of the nucleus.

Another mechanism that could result in net accumulation of Ca^{2+}-indicator complex is if the Ca^{2+}-bound form of the indicator is more permeable than the free indicator in the inward direction only, as might occur if the nuclear pore had different selectivities in different directions. Using computer modeling, we were able to get similar results to those shown in Fig. 7 *B* using indicator binding by making the permeability of the Ca^{2+}-indicator complex 20% larger in the inward direction than the outward direction (data not shown). However, we think this mechanism is unlikely as we also saw a larger fluorescence increase in the experiments with ionomycin than with electrical stimulation (1.38 ± 0.01, $n = 6$ vs. 1.15 ± 0.02, $n = 19$), whereas with the relative permeability mechanism, the ionomycin increases were not similarly enhanced (data not shown).

These passive mechanisms for the larger nuclear fluorescence increase occur due to the action of mobile Ca^{2+} buffers. In our experiments, the mobile Ca^{2+} buffers are introduced through the pipette, and endogenous mobile buffer washes out (Zhou and Neher, 1993), so the results could be considered an indicator-dependent artifact. However, the results shown in Fig. 7 *B* demonstrate how mobile buffers could generate a higher nuclear Ca^{2+} signal. To understand the physiological relevance, we would need to know more about the endogenous mobile buffers. In this regard it is interesting that Zhou and Neher (1993) reported that the endogenous mobile buffer variably contributes 0–50% of the total (mobile plus fixed) endogenous cellular buffer in different cells. In addition, several recent studies have indicated that cell stimulation can result in translocation of the Ca^{2+}-binding protein calmodulin to the nucleus (Craske et al., 1999; Deisseroth et al., 1998).

Nuclear Ca^{2+} signals generated by passive Ca^{2+} redistribution and different indicator properties in the nucleus

Finally, we also considered whether the higher fluorescence in the nucleus could be generated by a mechanism not involving a higher nuclear Ca^{2+} concentration, but due to different behavior of the Ca^{2+} indicator in the nucleus and the cytosol. Here, we also assume a passive diffusion of Ca^{2+} and indicator across the nuclear membrane.

Other studies have questioned whether different fluorescence changes in the cytosol and nucleus represent different Ca^{2+} concentration changes (Thomas et al., 2000). It has been suggested that the different magnitudes of the nuclear and cytosolic signals are due to differences in the indicator Ca^{2+} calibration parameters in the nucleus and the cytosol. One study reported that the dynamic range (F_{max}/F_{min}) of some, but not all, Ca^{2+} indicators is larger in the nucleus that the cytosol (Thomas et al., 2000). Thus, we considered a mechanism where the large fluorescence increase in the nucleus was due to a larger dynamic range of indicator fluorescence (F_{max}/F_{min}) in the nucleus than in the cytosol and not due to a difference in Ca^{2+} concentration. In this simulation (Fig. 7 *C*), the lag before the nuclear increase is obtained by assuming limited permeability of the nuclear pore for Ca^{2+} and Ca^{2+}-indicator complex. The dynamic range of the indicator had to be at least five times larger in the nucleus. This value is considerably larger than the largest difference in F_{max}/F_{min} measured by Thomas et al. (2000), which was about twofold for the indicator fluo-4 (they did not report values for rhod-2). These authors used the acetoxymethyl ester loading of the indicator, so it is possible, if not likely, that differences in compartmentalization and partial hydrolysis of the indicator are the cause of the different fluorescence properties of the indicator. In contrast, we loaded the acid form of the indicator through the patch pipette, a method that is less subject to such problems. However, although we typically observed a higher fluorescence of the nucleus than the cytosol in fluorescence images

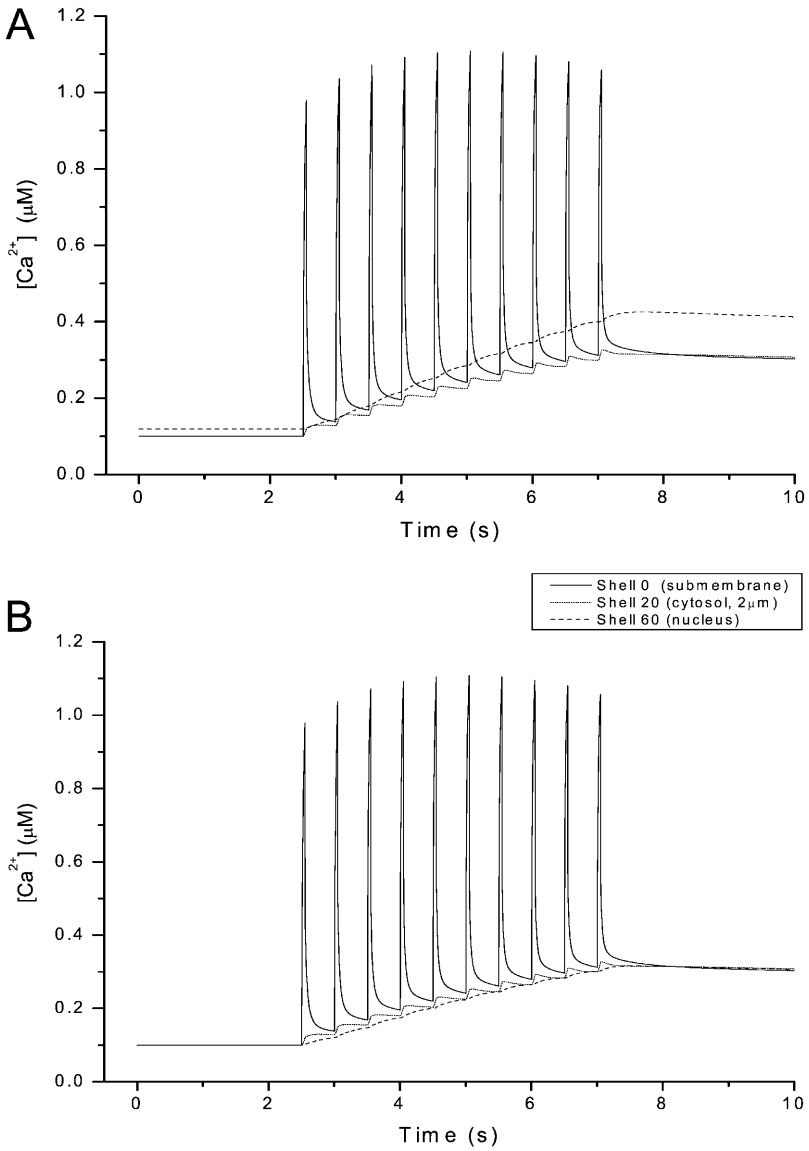

FIGURE 9 Simulation of dynamics of Ca^{2+} gradients during repetitive stimuli. Time courses of simulated changes in Ca^{2+} concentration for the models described in Fig. 7 and Methods. The different lines represent the time courses in the outer 100 nm shell (*solid line*), in a cytosolic shell 2 μm from the cell membrane (*dotted line*), and a nuclear shell (6 μm from the cell membrane, *dashed line*). (*A*). Simulation using the model described in Fig. 7 *B*, where the higher nuclear fluorescence is due to accumulation of bound Ca^{2+}-indicator complex in the nucleus. Note that the steady-state nuclear Ca^{2+} concentration is higher than the cytosolic Ca^{2+} concentration. (*B*) Simulation using the model described for Fig. 7 *C*, where the higher nuclear fluorescence is due to fluorescence properties of the Ca^{2+} indicator. Note the different dynamic patterns of response in the submembrane shell (large spikes), the cytosol (stepwise increases), and nucleus (gradual, delayed increase).

taken at rest, the difference is not as large as would be expected if the F_{max}/F_{min} of the indicator in the nucleus was >5 times than in the cytosol (data not shown). We think it is unlikely that this mechanism alone could account for the observed nuclear fluorescence signal. On the other hand, it is plausible that it might contribute in combination with binding in the nucleus, where the binding might be the cause of the different fluorescence behavior.

When we added ionomycin to patch-clamped chromaffin cells, to induce a spatially uniform increase in Ca^{2+} concentration, there was a larger F_t/F_o value in the nucleus than the cytosol measured after 3–10 min (4.3 $\pm$ 0.4 compared to 3.1 $\pm$ 0.3, $n = 6$). The larger change in the nucleus is consistent with the mechanism involving binding of the Ca^{2+}-indicator complex to nuclear constituents and consequent slow accumulation of Ca^{2+}-indicator complex (Fig. 8 *B*) or the mechanism where the indicator F_{max}/F_{min} was larger in the nucleus (Fig. 8 *C*). However, the observation that ionomycin gives a larger relative increase in the nucleus (1.38 $\pm$ 0.01, $n = 6$) than electrical stimulation (1.15 $\pm$ 0.02, $n = 19$) was better reproduced with the nuclear binding mechanism (see Fig. 8 *B*).

Limitations of the computer model

We have developed a mathematical computer model that can account for many properties of the Ca^{2+} changes that occur during single pulse and repetitive depolarizing stimuli and can be used as an investigative tool (see Conclusions). However, a computer simulation inevitably attempts to simulate a typical ''average'' cell. In developing the model, we have had to make a number of simplifications, notably spherical symmetry and homogeneity of the cell membrane, cytoplasmic and nuclear properties, which means that the model does not accurately

reproduce all the properties of the Ca^{2+} changes in real cells. First, real cells show considerable variation in the size of the Ca^{2+} changes, in part due to difference in the Ca^{2+} current but also due to other factors (e.g., buffer capacity). Second, the Ca^{2+} distribution is not spherically symmetrical. The Ca^{2+} gradients at the edge are not symmetrical (see Fig. 1) and we have previously noted this nonuniformity (Monck et al., 1994). We do not know if this difference is due to the number of Ca^{2+} channels or differences in local buffering. The nonuniformity is more apparent for short pulses and we suspect it is differences in channel density—we estimate that the differences of two- to threefold can explain the data. However, as the Ca^{2+} changes at the cell perimeter become more uniform at longer pulses (Monck et al., 1994) or after later pulses during a train of pulses (e.g., Figs. 1 and 2), the spherical assumption seems a reasonable approximation. Third, the region exhibiting the largest fluorescence change is off center due to the position of the nucleus, as seen in the images in Figs. 1, 2, and 8. With a radial diffusion model, we could only place the nucleus in the center. However, by increasing the size of the nucleus we could see the effect of the nucleus being closer to the cell membrane; predictably the cytosolic Ca^{2+} concentration away from the cell membrane increased faster. However, the same general pattern, where there are different dynamic changes in the Ca^{2+} concentration in the submembrane vicinity, the global cytosol, and the nucleus, was still observed. Thus, whereas the model makes various simplifying assumptions, it still can predict the general pattern of temporal and spatial Ca^{2+} changes in depolarization induced chromaffin cells.

CONCLUSIONS

We conclude that the slowly developing fluorescent increase seen in the center of the cell is due to a slowly developing Ca^{2+} increase in the nucleus, based on the following. First, the large fluorescence increase colocalizes with the nucleus as seen in bright-field images. Second, Ca^{2+} release from endoplasmic reticular or mitochondrial stores in the perinuclear region is unlikely to be involved, as blocking or depleting these stores had no affect on the observed Ca^{2+} changes. Third, computer simulations show several plausible mechanisms that explain how such a nuclear fluorescence increase can occur: a Ca^{2+} accumulation into the nucleus due to active Ca^{2+} transport mechanisms; a passive diffusional model involving accumulation of Ca^{2+}-indicator complex due to binding to nuclear constituents; or a passive diffusion model with different properties of the Ca^{2+} indicator in the nucleus.

Although we cannot offer a definitive mechanism for the larger fluorescence change measured in the nucleus, we favor the nuclear binding mechanism, as there is no strong evidence for active Ca^{2+} transport into the nucleus, and the binding mechanism explains the experiments with ionomycin better than the mechanism with different fluorescence of the indicator in the nucleus. However, it is also possible that such binding might cause changes in the fluorescence properties of the indicator that might contribute to the larger fluorescence change in the nucleus (i.e., a hybrid model). However, regardless of the exact mechanism, all three models can simulate the dynamics and spatial distribution of the observed fluorescence changes. One point we cannot distinguish is whether the absolute Ca^{2+} concentration is higher in the nucleus; with most mechanisms, the Ca^{2+} increase is larger in the nucleus, but in the case of the mechanism with different dye properties in the nucleus, the Ca^{2+} concentration is not higher. On the other hand, with all three cases, the fluorescence increase in the nucleus occurs more slowly and after a delay with respect to the fluorescence change in the cytosol. Thus, the fluorescent measurements do reflect the time course of the Ca^{2+} changes in the nucleus and all three models can simulate the dynamics and spatial distribution of the observed fluorescence changes.

Why build a virtual cell?

The combination of fluorescent measurements of the Ca^{2+} signal distribution and computer simulation allows us to build a more complete picture of the dynamic and spatial properties of the Ca^{2+} signal. Modeling alone is limited unless it can be shown to be relevant to physiological conditions. On the other hand, the types of data that may be measured are limited by a number of factors, limits in the spatial and temporal resolution of the measurements, and perturbation of the Ca^{2+} signals by the Ca^{2+} indicators. In addition, the measurements are restricted to a finite number of data points (times and locations).

By making measurements and using them to develop a ''virtual cell'' describing the dynamics of the measured Ca^{2+} distribution, we hope to gain the benefits of both methods. We can then use the model to interpolate to times between data points and to explore possibilities that are not subject to experimental determination. For example, we can predict what the Ca^{2+} signal might look like in the absence of the perturbing effects of the Ca^{2+} indicator (e.g., see Fig. 9 in Marengo and Monck (2000)).

Second, we can use the virtual cell as a tool to explore putative cellular mechanisms or possible artifactual behavior due to the indicator, as we have just done for the nuclear fluorescence increase. When we start considering the spatial distribution of Ca^{2+} signals, we must consider that measured fluorescence changes may be due to changes in Ca^{2+}, changes in distribution of the indicator, or changes in the properties of the Ca^{2+} indicator. Although we were unable to definitely assign a mechanism for the fluorescence increase in the nucleus, we were able to devise several plausible explanations. In addition, with all three mechanisms, the time course of the fluorescence changes appears to provide a reasonable estimate of the dynamics of the Ca^{2+} changes.

Finally, we can use the model to extrapolate to locations close to the membrane that are beyond the resolution of light microscope. Fig. 9 shows the simulated time courses of the Ca^{2+} signal for a shell within 100 nm of the cell membrane and compares this with the time courses at several locations within the cytosol and within the nucleus. The figure shows simulations using models where the higher nuclear fluorescence is due to accumulation of bound Ca^{2+}-indicator complex in the nucleus (*A*) and different fluorescence properties of the Ca^{2+} indicator in the nucleus (*B*), as described in for the simulations shown in Fig. 7, *B* and *C*, respectively. These simulations illustrate how Ca^{2+} entry in response to repetitive depolarizing stimuli can generate distinct Ca^{2+} signals with different dynamic properties—a relatively large and rapid transient submembrane signal, a stepwise cytosolic Ca^{2+} signal, and a slower, delayed rise in the nuclear compartment.

Together, these arguments explain why the combined use of Ca^{2+} measurements and computer simulation of ''virtual cells'' is now being used to study many aspects of Ca^{2+} signaling, including Ca^{2+} sparks formation (Smith et al., 1998), Ca^{2+} wave propagation (Fink et al., 2000), Ca^{2+} gradients associated with exocytosis (Issa and Hudspeth, 1996; Marengo and Monck, 2000), and Ca^{2+} gradients within sarcomers (DiFranco et al., 2002).

Physiological consequences

The compartmentalization of the Ca^{2+} signal, in terms of its dynamic and spatial properties, allows a cell to use a single intracellular signaling molecule to distinctly regulate many different processes. The experimental data and model simulations illustrate how Ca^{2+} entry in response to repetitive stimuli can generate three distinct Ca^{2+} signals with different dynamic properties. Comparison of the time course of these different ''Ca^{2+} signals''—submembrane, cytosolic, and nuclear—show that they respond distinctly to different stimulus patterns (see Fig. 9). Thus a single pulse gives a submembrane gradient and a small ''global'' cytosolic signal, but nothing significant in the nucleus. This would be an appropriate signal to stimulate fusion of docked fusion-ready chromaffin granules. This type of stimulus causes release of an ''immediately releasable'' pool of granules (e.g., Heinemann et al., 1993; Horrigan and Bookman, 1994). Repeating the depolarizing pulses starts giving a stepwise increment of the cytosolic Ca^{2+}, which is approximately proportional to the number of pulses, but there is still only a comparatively small change in the nucleus. This signal would be appropriate for mobilizing more granules to the releasable pool and stimulating other cytosolic functions that might be necessary for granule recruitment and priming, as well as for endocytic membrane retrieval (Artalejo et al., 1996). It is an interest in the relative role of submembrane and so-called ''residual'' Ca^{2+} signals in regulating membrane fusion, facilitation, and vesicle mobilization that led us to the current study. Finally, a longer train of repetitive pulses also starts to give a prominent increase in the nucleus. Thus strong repetitive stimulation of a chromaffin cell, which would be expected to cause large amounts of exocytosis, would also initiate Ca^{2+}-dependent processes in the nucleus (Craske et al., 1999; Deisseroth et al., 1996, 1998), leading to stimulation of transcription and synthesis of granule proteins and enzymes necessary for formation of new secretory granules. The role of the submembrane and cytosolic Ca^{2+} signals in regulation chromaffin granule fusion and mobilization will be the subject of a future article.

We thank Dr. David DiGregorio for many interesting discussions on cellular Ca^{2+} buffering, Ca^{2+} measurements, and modeling of the Ca^{2+} gradients. Special thanks are due to Dr. Bernard Ribalet for critical reading of the manuscript. We also thank Dr. Dan Ungureanu for assistance with Fig. 6.

This work was supported by grant GM54340 (to J.R.M.) from the National Institutes of Health.

REFERENCES

al-Mohanna, F. A., K. W. Caddy, and S. R. Bolsover. 1994. The nucleus is insulated from large cytosolic calcium ion changes. *Nature*. 367:745–750.

Artalejo, C. R., A. Elhamdani, and H. C. Palfrey. 1996. Calmodulin is the divalent cation receptor for rapid endocytosis, but not exocytosis, in adrenal chromaffin cells. *Neuron*. 16:195–205.

Baylor, S. M., and S. Hollingworth. 1988. Fura-2 calcium transients in frog skeletal muscle fibres. *J Physiol*. 403:151–192.

Berridge, M. J., P. Lipp, and M. D. Bootman. 2000. The versatility and universality of calcium signalling. *Nat. Rev. Mol. Cell Biol*. 1:11–21.

Brini, M., and E. Carafoli. 2000. Calcium signalling: a historical account, recent developments and future perspectives. *Cell. Mol. Life Sci*. 57:354–370.

Burgoyne, R. D., T. R. Cheek, A. Morgan, A. J. O'Sullivan, R. B. Moreton, M. J. Berridge, A. M. Mata, J. Colyer, A. G. Lee, and J. M. East. 1989. Distribution of two distinct $Ca2^{+}$-ATPase-like proteins and their relationships to the agonist-sensitive calcium store in adrenal chromaffin cells. *Nature*. 342:72–74.

Burgoyne, R. D., and M. J. Geisow. 1989. The annexin family of calcium-binding proteins. Review article. *Cell Calcium*. 10:1–10.

Burgoyne, R. D., A. Morgan, and A. J. O'Sullivan. 1988. A major role for protein kinase C in calcium-activated exocytosis in permeabilised adrenal chromaffin cells. *FEBS Lett*. 238:151–155.

Craske, M., T. Takeo, O. Gerasimenko, C. Vaillant, K. Torok, O. H. Petersen, and A. V. Tepikin. 1999. Hormone-induced secretory and nuclear translocation of calmodulin: oscillations of calmodulin concentration with the nucleus as an integrator. *Proc. Natl. Acad. Sci. USA*. 96:4426–4431.

Deisseroth, K., H. Bito, and R. W. Tsien. 1996. Signaling from synapse to nucleus: postsynaptic CREB phosphorylation during multiple forms of hippocampal synaptic plasticity. *Neuron*. 16:89–101.

Deisseroth, K., E. K. Heist, and R. W. Tsien. 1998. Translocation of calmodulin to the nucleus supports CREB phosphorylation in hippocampal neurons. *Nature*. 392:198–202.

DiFranco, M., D. Novo, and V. L. Vergara. 2002. Characterization of the calcium release domains during excitation-contraction coupling in skeletal muscle fibres. *Pflugers Arch*. 443:508–519.

DiGregorio, D. A., A. Peskoff, and J. L. Vergara. 1999. Measurement of action potential-induced presynaptic calcium domains at a cultured neuromuscular junction. *J. Neurosci*. 19:7846–7859.

DiGregorio, D. A., and J. L. Vergara. 1997. Localized detection of action potential-induced presynaptic calcium transients at a Xenopus neuromuscular junction. *J. Physiol. (Lond.).* 505:585–592.

Escobar, A. L., J. R. Monck, J. M. Fernandez, and J. L. Vergara. 1994. Localization of the site of $Ca2^+$ release at the level of a single sarcomere in skeletal muscle fibres. *Nature.* 367:739–741.

Escobar, A. L., P. Velez, A. M. Kim, F. Cifuentes, M. Fill, and J. L. Vergara. 1997. Kinetic properties of DM-nitrophen and calcium indicators: rapid transient response to flash photolysis. *Pflugers Arch.* 434:615–631.

Fink, C. C., B. Slepchenko, I. I. Moraru, J. Watras, J. C. Schaff, and L. M. Loew. 2000. An image-based model of calcium waves in differentiated neuroblastoma cells. *Biophys. J.* 79:163–183.

Gabso, M., E. Neher, and M. E. Spira. 1997. Low mobility of the $Ca2^+$ buffers in axons of cultured Aplysia neurons. *Neuron.* 18:473–481.

Gerasimenko, O. V., J. V. Gerasimenko, A. V. Tepikin, and O. H. Petersen. 1995. ATP-dependent accumulation and inositol trisphosphate- or cyclic ADP- ribose-mediated release of $Ca2^+$ from the nuclear envelope. *Cell.* 80:439–444.

Gerasimenko, O. V., J. V. Gerasimenko, A. V. Tepikin, and O. H. Petersen. 1996. Calcium transport pathways in the nucleus. *Pflugers Arch.* 432: 1–6.

Harkins, A. B., N. Kurebayashi, and S. M. Baylor. 1993. Resting myoplasmic free calcium in frog skeletal muscle fibers estimated with fluo-3. *Biophys. J.* 65:865–881.

Heinemann, C., L. von Ruden, R. H. Chow, and E. Neher. 1993. A two-step model of secretion control in neuroendocrine cells. *Pflugers Arch.* 424:105–112.

Heizmann, C. W. 1992. Calcium-binding proteins: basic concepts and clinical implications. *Gen. Physiol. Biophys.* 11:411–425.

Hernández-Cruz, A., F. Sala, and P. R. Adams. 1990. Subcellular calcium transients visualized by confocal microscopy in a voltage-clamped vertebrate neuron. *Science.* 247:858–862.

Herrington, J., Y. B. Park, D. F. Babcock, and B. Hille. 1996. Dominant role of mitochondria in clearance of large $Ca2^+$ loads from rat adrenal chromaffin cells. *Neuron.* 16:219–228.

Horrigan, F. T., and R. J. Bookman. 1994. Releasable pools and the kinetics of exocytosis in adrenal chromaffin cells. *Neuron.* 13:1119–1129.

Iida, S. 1988. Calcium binding to troponin C. II. A $Ca2^+$ ion titration study with a $Ca2^+$ ion sensitive electrode. *J. Biochem. (Tokyo).* 103:482–486.

Issa, N. P., and A. J. Hudspeth. 1996. The entry and clearance of $Ca2^+$ at individual presynaptic active zones of hair cells from the bullfrog's sacculus. *Proc. Natl. Acad. Sci. USA.* 93:9527–9532.

Klingauf, J., and E. Neher. 1997. Modeling buffered $Ca2^+$ diffusion near the membrane: implications for secretion in neuroendocrine cells. *Biophys. J.* 72:674–690.

Konishi, M., A. Olson, S. Hollingworth, and S. M. Baylor. 1988. Myoplasmic binding of fura-2 investigated by steady-state fluorescence and absorbance measurements. *Biophys. J.* 54:1089–1104.

Leathers, V. L., S. Linse, S. Forsén, and A. W. Norman. 1990. Calbindin-D28K, a 1 α,25-dihydroxyvitamin D3-induced calcium-binding protein, binds five or six $Ca2^+$ ions with high affinity. *J. Biol. Chem.* 265:9838–9841.

Marengo, F. D., and J. R. Monck. 2000. Development and dissipation of $Ca2^+$ gradients in adrenal chromaffin cells. *Biophys. J.* 79:1800–1820.

Minta, A., J. P. Kao, and R. Y. Tsien. 1989. Fluorescent indicators for cytosolic calcium based on rhodamine and fluorescein chromophores. *J. Biol. Chem.* 264:8171–8178.

Monck, J. R., A. F. Oberhauser, T. J. Keating, and J. M. Fernandez. 1992. Thin-section ratiometric $Ca2^+$ images obtained by optical sectioning of fura-2 loaded mast cells. *J. Cell Biol.* 116:745–759.

Monck, J. R., E. E. Reynolds, A. P. Thomas, and J. R. Williamson. 1988. Novel kinetics of single cell $Ca2^+$ transients in stimulated hepatocytes and A10 cells measured using fura-2 and fluorescent videomicroscopy. *J. Biol. Chem.* 263:4569–4575.

Monck, J. R., I. M. Robinson, A. L. Escobar, J. L. Vergara, and J. M. Fernandez. 1994. Pulsed laser imaging of rapid $Ca2^+$ gradients in excitable cells. *Biophys. J.* 67:505–514.

Morimoto, S., and I. Ohtsuki. 1994. $Ca2^+$ binding to cardiac troponin C in the myofilament lattice and its relation to the myofibrillar ATPase activity. *Eur. J. Biochem.* 226:597–602.

Neher, E. 1992. Correction for liquid junction potentials in patch clamp experiments. *Methods Enzymol.* 207:123–131.

Nicotera, P., D. J. McConkey, D. P. Jones, and S. Orrenius. 1989. ATP stimulates $Ca2^+$ uptake and increases the free $Ca2^+$ concentration in isolated rat liver nuclei. *Proc. Natl. Acad. Sci. USA.* 86:453–457.

Nohmi, M., S. Y. Hua, and K. Kuba. 1992. Intracellular calcium dynamics in response to action potentials in bullfrog sympathetic ganglion cells. *J Physiol.* 458:171–190.

Nowycky, M. C., and M. J. Pinter. 1993. Time courses of calcium and calcium-bound buffers following calcium influx in a model cell. *Biophys. J.* 64:77–91.

Olwin, B. B., and D. R. Storm. 1985. Calcium binding to complexes of calmodulin and calmodulin binding proteins. *Biochemistry.* 24:8081–8086.

O'Sullivan, A. J., T. R. Cheek, R. B. Moreton, M. J. Berridge, and R. D. Burgoyne. 1989. Localization and heterogeneity of agonist-induced changes in cytosolic calcium concentration in single bovine adrenal chromaffin cells from video imaging of fura-2. *EMBO J.* 8:401–411.

Pan, C. Y., and L. S. Kao. 1997. Catecholamine secretion from bovine adrenal chromaffin cells: the role of the $Na^+/Ca2^+$ exchanger and the intracellular $Ca2^+$ pool. *J. Neurochem.* 69:1085–1092.

Pusch, M., and E. Neher. 1988. Rates of diffusional exchange between small cells and a measuring patch pipette. *Pflugers Arch.* 411:204–211.

Sala, F., and A. Hernández-Cruz. 1990. Calcium diffusion modeling in a spherical neuron. Relevance of buffering properties. *Biophys. J.* 57: 313–324.

Segal, M., and D. Manor. 1992. Confocal microscopic imaging of $[Ca2^+]i$ in cultured rat hippocampal neurons following exposure to N-methyl-D-aspartate. *J Physiol.* 448:655–676.

Smith, G. D., J. E. Keizer, M. D. Stern, W. J. Lederer, and H. Cheng. 1998. A simple numerical model of calcium spark formation and detection in cardiac myocytes. *Biophys. J.* 75:15–32.

Stehno-Bittel, L., C. Perez-Terzic, and D. E. Clapham. 1995. Diffusion across the nuclear envelope inhibited by depletion of the nuclear $Ca2^+$ store. *Science.* 270:1835–1838.

Tang, Y. M., E. R. Travis, R. M. Wightman, and A. S. Schneider. 2000. Sodium-calcium exchange affects local calcium signal decay and the rate of exocytotic secretion in single chromaffin cells. *J. Neurochem.* 74:702–710.

Teleman, O., T. Drakenberg, S. Forsen, and E. Thulin. 1983. Calcium and cadmium binding to troponin C. Evidence for cooperativity. *Eur. J. Biochem.* 134:453–457.

Thomas, D., S. C. Tovey, T. J. Collins, M. D. Bootman, M. J. Berridge, and P. Lipp. 2000. A comparison of fluorescent $Ca2^+$ indicator properties and their use in measuring elementary and global $Ca2^+$ signals. *Cell Calcium.* 28:213–223.

Williams, D. A., K. E. Fogarty, R. Y. Tsien, and F. S. Fay. 1985. Calcium gradients in single smooth muscle cells revealed by the digital imaging microscope using Fura-2. *Nature.* 318:558–561.

Zhou, Z., and E. Neher. 1993. Mobile and immobile calcium buffers in bovine adrenal chromaffin cells. *J. Physiol. (Lond.).* 469:245–273.